

Synthesis of cluster-derived PtFe/SiO₂ catalysts for the oxidation of CO

Attilio Siani^a, Oleg S. Alexeev^{a,*}, Burjor Captain^b, Gwendoline Lafaye^c, Patrice Marécot^c,
Richard D. Adams^b, Michael D. Amiridis^{a,*}

^a Department of Chemical Engineering, University of South Carolina, Columbia, SC 29208, USA

^b Department of Chemistry and Biochemistry, University of South Carolina, Columbia, SC 29208, USA

^c Laboratoire de Catalyse en Chimie Organique, UMR CNRS 6503 Université de Poitiers, 40 Avenue du Recteur Pineau, F-86022 Poitiers Cedex, France

Received 3 September 2007; revised 22 January 2008; accepted 26 January 2008

Available online 14 March 2008

Abstract

Infrared (FTIR) and extended X-ray absorption fine structure (EXAFS) spectroscopy measurements were used to characterize the species formed after impregnation of Pt₅Fe₂(COD)₂(CO)₁₂ onto silica, before and after removal of the organic ligands. The results indicate that the Pt₅Fe₂(COD)₂(CO)₁₂ cluster adsorbs weakly on the SiO₂ surface. Nevertheless, partial disintegration of the cluster was observed during aging even under He and at room temperature, related to the loss of CO ligands due to their interactions with silanol groups of the support. The organic ligands can be removed from a freshly impregnated cluster by thermal treatment in either He or H₂, but the surface species formed in each case have different structures. Treatment in He at 350 °C leads to a complete disintegration of the Pt–Fe bimetallic core and results in the formation of highly dispersed Pt clusters with a nuclearity of six, along with surface Fe oxide-like species. In contrast, bimetallic PtFe nanoparticles with an average size of approximately 1 nm were formed when a similar H₂ treatment was used. In this case, a greater degree of metal dispersion and a larger fraction of Pt–Fe interactions were observed compared to the PtFe/SiO₂ samples prepared by co-impregnation of monometallic salt precursors. Electronic interactions between Pt and Fe atoms in such cluster-derived samples led to an increased electron density on platinum, as indicated by a red shift of the frequencies of FTIR bands for adsorbed NO and CO. These electronic interactions affect the strength of the CO adsorption on platinum. All bimetallic samples were found to be more active than Pt/SiO₂ for the oxidation of CO in air; however, the activity depends strongly on the structure of the surface species, the fraction of Pt–Fe bimetallic contributions, the degree of electronic interactions between Pt and Fe, and the strength of the CO adsorption on platinum.

© 2008 Elsevier Inc. All rights reserved.

Keywords: Platinum; Iron; Bimetallic structures; EXAFS; CO oxidation

1. Introduction

Research conducted with supported bimetallic catalysts for several years has led to the recognition that their activity and/or selectivity are often greater than the simple sums of the properties of the two constituent metals, an effect known as “synergy” between the two metals [1–6]. The properties of bimetallic catalysts can be dramatically affected by the size and composition of their metal particles, the interactions of such particles with the support, and the interactions between the metals. The research interest in such materials continues to grow, because

various bimetallic combinations have been found to be important for large-scale industrial applications [1]. Several attempts have been made to elucidate the nature of the catalytic action and the origin of the synergistic effects for these complex materials. Based on density functional theory (DFT) calculations, it has been suggested that strain effects and electronic interactions between the constituent metals are crucial factors contributing to modification of the catalytic properties in bimetallic systems [7–9]. For example, the differences in the lattice constants between Pt and 3d transition metals (e.g., Cr, Fe, Co, and Ni) can lead to the formation of strained PtM bimetallic structures. DFT calculations showed that even on monometallic Ru(0001) surfaces, the presence of strains has a significant influence on their chemical properties due to a shift in the center of the metal *d* bands, which depends on the type of the strain [7]. Further-

* Corresponding authors.

E-mail addresses: alexeev@engr.sc.edu (O.S. Alexeev),
amiridis@engr.sc.edu (M.D. Amiridis).

more, DFT calculations also have shown that the presence of subsurface $3d$ transition metal atoms can significantly modify the electronic and chemical properties of a Pt(111) surface even in the absence of lateral strain [8,9]. In this case, the surface Pt d -band center was found to be of lower energy, with the magnitude of the effect increasing as the nature of the subsurface $3d$ metal was changed from Ni to Ti [8]. The dissociative adsorption energies of H_2 , O_2 , and CO were found to be lower as a result of this shift [8,9], thus affecting the surface coverage of such species and the availability of active metal sites.

Despite these advances, much remains to be learned about the nature and stability of bimetallic structures, especially during the course of chemical reactions. Conventional preparation techniques, frequently used for the preparation of such catalysts, usually lead to nonuniform materials and provide limited control over the composition of the bimetallic species formed. This has motivated researchers to investigate various model catalysts, such as those derived from bimetallic clusters supported on high-surface area supports. Although a wide variety of clusters with well-defined mixed-metal cores stabilized by various organic ligands are known, only a limited number of them have been used as precursors for the preparation of supported catalysts [10]. Among these, examples incorporating Fe constitute only a small fraction, limited to Fe–Ru, Fe–Pt, Fe–Rh, Fe–Mo, Fe–Mn, Fe–Pd, Fe–Os, Fe–Co, and Fe–Ir combinations [10]. The resulting catalysts in these cases can catalyze reactions occurring in highly reducing environments, such as CO hydrogenation, hydrodesulfurization, hydrocarbon skeletal rearrangements, olefin hydroformylation, and the preferential oxidation of CO [10–12].

The goal of the present work was to prepare and characterize SiO_2 -supported Pt–Fe catalysts using a $Pt_5Fe_2(COD)_2(CO)_{12}$ precursor that contains well-defined Pt–Fe bonds. In this paper, we examine the structural changes occurring during the interaction of the $Pt_5Fe_2(COD)_2(CO)_{12}$ cluster with the surface of SiO_2 and the subsequent ligand removal steps. Fourier transform infrared (FTIR) and extended X-ray absorption fine structure (EXAFS) spectroscopy were used to characterize the surface species. The evolution of CO ligands during decarbonylation was monitored to gain insight into the parameters of the ligand removal process, and the catalytic properties of the decarbonylated samples were evaluated for the oxidation of CO in air.

2. Experimental

2.1. Reagents and materials

$H_2PtCl_6 \cdot 6H_2O$ (99% purity, Alfa Aesar) and $Fe(NO_3)_3 \cdot 9H_2O$ (99% purity, Fisher Scientific) were used as supplied. The $Pt_5Fe_2(COD)_2(CO)_{12}$ cluster was prepared under dry N_2 using standard Schlenk techniques as described previously [11,12]. The SiO_2 support (100 m^2/g ; Engelhard) was calcined overnight in air at 500 °C and then partially dehydroxylated by a vacuum treatment at 500 °C for 24 h and stored in a dry box (MBraun). A dry methylene chloride solvent (Fisher Scientific) was used without additional purification. N_2 , H_2 , He, and the

CO/N_2 mixture (all UHP grade, Airstar) were also purified before use by passing them through oxygen/moisture traps (Agilent) capable of removing traces of O_2 and water to 15 and 25 ppb, respectively. In addition, the CO/N_2 mixture was heated to 350 °C in a trap filled with quartz particles (60–80 mesh), to eliminate any metal carbonyls that may have formed in the storage cylinder.

2.2. Sample preparation

Pt_5Fe_2/SiO_2 was prepared by slurring the $Pt_5Fe_2(COD)_2(CO)_{12}$ (COD: 1,5-cyclooctadiene) precursor in CH_2Cl_2 with the powdered SiO_2 support at room temperature for 24 h under nitrogen flow, as reported elsewhere [12]. The solvent was subsequently removed by evacuation at room temperature, and the sample was stored in a dry box filled with N_2 . The residual water and O_2 concentrations in the dry box were kept below 0.1 ppm, to prevent possible decomposition of the supported species. The amount of the precursor was chosen to yield samples containing 1.0 wt% Pt and 0.11 wt% Fe after ligand removal. A reference 1.0 wt% Pt/ SiO_2 sample was prepared by conventional incipient wetness impregnation of SiO_2 with an aqueous solution of $H_2PtCl_6 \cdot 6H_2O$. In addition, a bimetallic sample containing 1.0 wt% Pt and 0.11 wt% Fe (designated PtFe/ SiO_2) was also prepared for comparison purposes by incipient wetness impregnation of SiO_2 with an aqueous solution containing a mixture of $H_2PtCl_6 \cdot 6H_2O$ and $Fe(NO_3)_3 \cdot 9H_2O$. The Pt and Fe weight loadings in all samples were verified by inductively coupled plasma–mass spectroscopy (ICP-MS) analysis (Galbraith Laboratories).

2.3. FTIR spectroscopy

A Thermo Nicolet Nexus 470 spectrometer was used to record spectra with a resolution of 2 cm^{-1} , averaging 64 scans per spectrum. Powder samples were pressed into self-supported wafers of nearly the same density (20 mg/cm^2) and thickness under 5000 psi of pressure. The wafers were then mounted in a homemade IR cell connected to a gas distribution manifold [13]. The cell construction allowed for treatment of the samples at different temperatures while various gases were flowed through the cell. IR spectra for different samples were compared assuming that the extinction coefficient for a given adsorbed species remained unchanged from sample to sample.

2.4. Temperature-programmed desorption of CO ligands

For each set of temperature-programmed desorption (TPD) measurements, approximately 100 mg of powdered fresh catalyst was mixed with 7 g of inert quartz powder (60–80 mesh) and loaded into a fixed-bed quartz reactor. The reactor was heated to 400 °C at a rate of 3 °C/min with He or H_2 flowing through at a rate of 100 cc/min. The concentration of CO in the effluent gas mixture was monitored with a Siemens Ultramat 23 online single-beam NDIR analyzer capable of detecting CO in the 0–500 ppm and 0–5% ranges. The evolution of CO_2 was

monitored by an online gas chromatography system equipped with a thermal conductivity detector.

2.5. H_2 chemisorption

A Micromeritics ChemiSorb 2720 pulse analyzer was used to measure the accessibility of surface sites by hydrogen chemisorption at room temperature.

2.6. EXAFS spectroscopy

EXAFS spectra were collected at X-ray beamline 2–3 at the Stanford Synchrotron Radiation Laboratory, Stanford Linear Accelerator Center, Menlo Park, CA. The storage ring electron energy was 3 GeV, and the ring current was in the range of 80–100 mA.

All samples examined were pretreated in a glass reactor with H_2 or He at the desired temperature to remove the ligands. After the completion of the treatment, the reactor was sealed and transferred into a dry box, where samples were loaded into an EXAFS cell in a powder form. The EXAFS cell design allows handling of samples without air exposure. The EXAFS data were recorded at room temperature in the fluorescence mode with a 13th element Ge detector due to the low Fe loading. The total count rate for the Ge detector was in the range of 30,000–40,000 counts/s. It has been experimentally established that the detector readings are linear within this range and that no corrections for any dead-time are required. Samples were scanned at both the Pt L_3 edge (11564 eV) and the Fe K edge (7112 eV). Data were collected with a Si(220) double-crystal monochromator, which was detuned by 30% to minimize the effects of higher harmonics in the X-ray beam.

2.7. CO oxidation measurements

Catalytic activity measurements for the oxidation of CO in air were performed in a quartz single-pass, fixed-bed reactor at atmospheric pressure and at 25–300 °C. The temperature inside the reactor was monitored by a thermocouple extended into the catalyst bed. Samples in powder form (0.077 g) were diluted 90 times by weight with quartz particles (60–80 mesh) to keep the catalyst bed isothermal. The total volumetric flow rate of the reactant mixture (1% CO in air) was held at 154 ml/min (1 atm, 25 °C), yielding a corresponding gas hourly space velocity (GHSV) of 120,000 ml/g h. The feed and reaction products were analyzed with a Siemens Ultramat 23 online single-beam NDIR CO analyzer capable of detecting CO in the 0–500 ppm and 0–5% ranges and CO_2 in the 0–5% range.

Before catalytic measurements, all samples were treated with H_2 or He while the temperature was ramped at 5 °C/min to 350 °C and held at this temperature for 2 h. After the treatment was completed, the reactor was purged with He at 350 °C and cooled to room temperature. The reaction mixture was introduced at that point and data were collected at different times, with the temperature raised every 2 h in 10–20 °C increments. In the absence of a catalyst, no measurable conversion of CO was observed.

2.8. EXAFS data analysis

The EXAFS data were analyzed with a combination of experimental and theoretical reference files. The former were obtained from EXAFS data collected for materials with known structures. More specifically, the Pt–Pt, Pt– O_{support} , Pt–CO, and Fe– O_{support} interactions were analyzed with phase shifts and backscattering amplitudes obtained from EXAFS data for Pt foil, $Na_2Pt(OH)_6$, $Ir_4(CO)_{12}$, and FeO, respectively. It has been shown both theoretically and experimentally that Ir references can be used to analyze Pt data [14,15]. EXAFS data obtained for Fe foil cannot be used directly for the analysis of metal–metal contributions at the Fe edge because the Fe foil has a bcc structure in which the first and second Fe–Fe shells are not resolved; therefore, the first shell Fe–Fe contributions were isolated by modeling the spectrum of the Fe bcc structure with the FEFF8 software and assuming the presence of only 8 Fe atoms in positions corresponding to the first coordination shell. The Fe–CO, Pt–Fe, and Fe–Pt interactions were analyzed with phase shifts and backscattering amplitudes calculated with the FEFF8 software on the basis of the crystallographic data reported for $Fe(CO)_5$ [16] and $PtFe(CO)_3(COD)[\mu\text{-PhCC(H)C(H)CPh}]$ [11], respectively. The crystallographic first-shell coordination parameters for all the reference compounds, the weighting of the Fourier transform, and the ranges in k and r space used to extract the reference functions from the experimental EXAFS data are given in Table 1. The EXAFS parameters were extracted from the raw data using the XDAP software developed by XAFS Services International [17]. The methods used to extract the EXAFS function from the raw data are essentially the same as those reported elsewhere [18]. Data reported for each sample are the averages of six scans.

The raw EXAFS data obtained for the Pt L_3 and Fe K edges were analyzed with a maximum number of free parameters not exceeding the statistically justified number of free parameters, n , estimated based on the Nyquist theorem [19,20]: $n = (2\Delta k \Delta r / \pi) + 1$, where Δk and Δr are the k (where k is the wave vector) and r (where r is the distance from the absorber atom) ranges used to fit the data. The statistically justified number of free parameters and the ranges of k and r used for each fit are reported as notations in the tables containing the EXAFS data. The data analysis was performed with a difference file technique with phase- and amplitude-corrected Fourier transforms of the data [21,22].

The approach used to analyze the data for bimetallic samples at the Pt L_3 edge was similar to that described previously [23]. The Pt–Pt contributions in each sample (the largest in the EXAFS spectra) were estimated first and then subtracted from the raw data. The difference file was expected to represent Pt– O_{support} contributions. After optimizing the parameters for the Pt– O_{support} contributions, the first-guess Pt–Pt and Pt– O_{support} contributions were added and compared with the raw data. The overall fit with the sum of the Pt–Pt and Pt– O_{support} contributions was not satisfactory. The difference file obtained after subtraction of the Pt–Pt and Pt– O_{support} contributions from the raw data indicated the presence of additional

Table 1
Structural parameters characterizing the reference compounds and Fourier transform ranges used in the EXAFS data analysis^a

Shell	<i>N</i>	<i>R</i> (Å)	<i>n</i>	Δk	Δr (Å)	Reference compound
Pt–Pt	12	2.77	3	1.9–19.8	1.9–3.0	Pt foil
Fe–Fe	8	2.49	3	1.5–19.0	1.1–2.4	Fe foil ^b
Pt–O	6	2.05	3	1.4–17.7	0.5–2.0	Na ₂ Pt(OH) ₆
Ir–C	3	1.87	3	2.8–16.5	1.1–2.0	Ir ₄ (CO) ₁₂
Ir–O	3	3.01	3	2.8–16.5	2.0–3.3	
Fe–O	6	2.15	2	1.4–16.5	0.5–2.0	FeO
Fe–C	5	1.81	3	2.0–16.5	0.5–2.6	Fe(CO) ₅ ^b
Fe–O	5	2.93	3	2.0–16.5	2.0–3.3	
Pt–Fe	1	2.83	3	2.0–17.5	1.9–3.5	PtFe(CO) ₃ (COD)[PhCC(H)C(H)CPh] ^b
Fe–Pt	1	2.83	3	2.0–17.5	1.9–3.5	

^a Notation: *N*, coordination number for absorber-backscatterer pair; *R*, distance; Δk , limits used for forward Fourier transform (*k* is the wave vector); Δr , limits used for the shell isolation (*r* is the distance); *n*, power of *k* used in the Fourier transformations.

^b A theoretical EXAFS function was calculated with FEFF8 software.

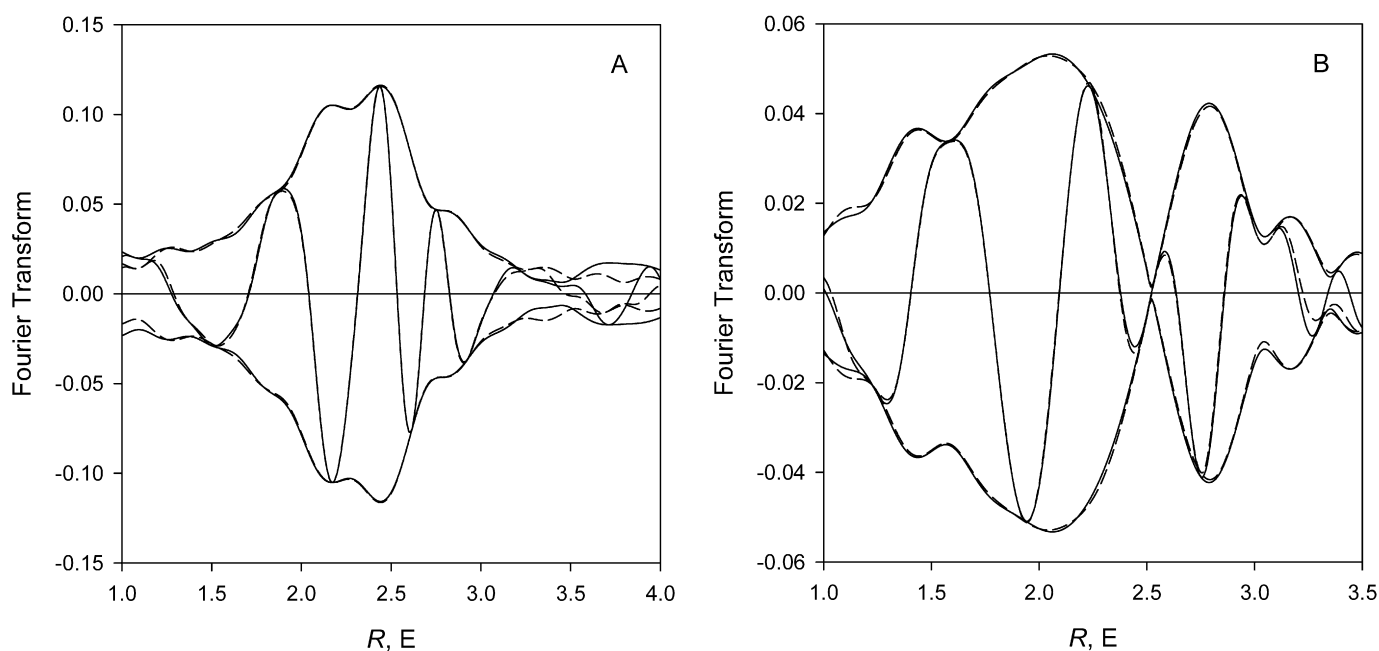


Fig. 1. Results of EXAFS analysis of a Pt₅Fe₂(COD)₂(CO)₁₂/SiO₂ sample treated in H₂ at 350 °C: imaginary part and magnitude of uncorrected Fourier transform (*k*¹ weighted) of experimental EXAFS (solid line) and sum of the calculated contributions as stated in Table 6 (dashed line) for the Pt L₃ (A) and Fe K (B) edges.

high-*Z* backscatters, which in this case appeared to be Pt–Fe. Therefore, a good fit at the Pt L₃ edge was obtained when all Pt–Pt, Pt–Fe, and Pt–O_{support} contributions were accounted for. The difference file in this case showed only the presence of noise, indicating that no other contributions had to be included in the fit.

A similar approach was used to analyze the EXAFS data at the Fe K edge, with the best fit obtained when Fe–Pt and Fe–O_{support} contributions were used for the data analysis. Reliable parameters for the high-*Z* (Pt, Fe) and low-*Z* (O_{support}) contributions were determined by multiple-shell fitting in *r* space with application of *k*¹ and *k*³ weightings in the Fourier transformations [18]. Because the EXAFS data were obtained at both the Pt L₃ edge and the Fe K edge, there were opportunities to evaluate the internal consistency of the fitting results, as described below. Comparisons of the data and fits in *r*-space for two selected samples are shown in Figs. 1 and 2; the best-fitting

parameters determined by this fitting routine for all samples investigated are summarized in Tables 2, 5, 6, and 8. Standard deviations reported in these tables for the various parameters were calculated from the covariance matrix taking into account the statistical noise of the EXAFS data and the correlations between the different coordination parameters, as described elsewhere [24]. Systematic errors are not included in the calculation of the standard deviations. The goodness-of-fit values (ϵ_v^2) were calculated as outlined in [25]. The variances in both the imaginary and absolute parts were used to determine the quality of the fit [26].

2.9. XANES measurements and analysis

X-ray absorption near-edge (XANES) spectra of each sample were also obtained during the X-ray absorption measurements described above. Normalized XANES spectra were ob-

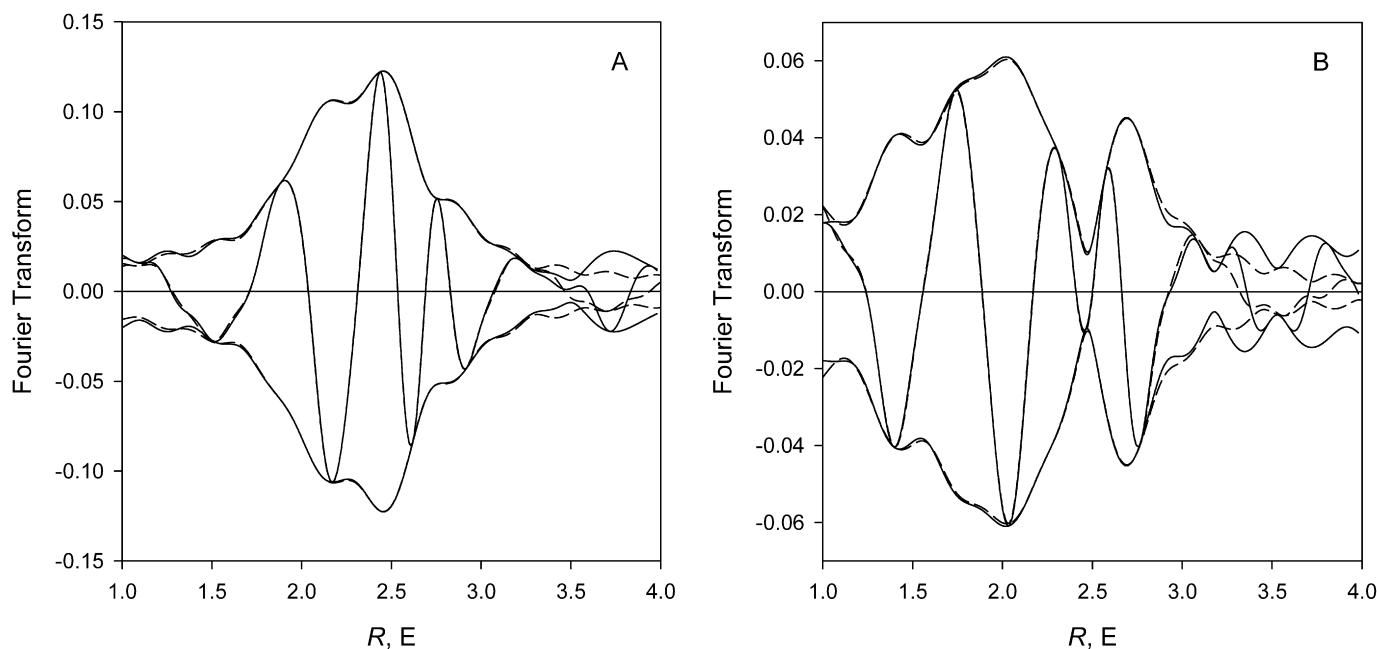


Fig. 2. Results of EXAFS analysis of a PtFe/SiO₂ sample treated in H₂ at 350 °C: imaginary part and magnitude of uncorrected Fourier transform (k^1 weighted) of experimental EXAFS (solid line) and sum of the calculated contributions as stated in Table 8 (dashed line) for the Pt L_3 (A) and Fe K (B) edges.

Table 2
EXAFS parameters characterizing Pt₅Fe₂(COD)₂(CO)₁₂/SiO₂ after aging in He at room temperature for 5 days^a

Edge	Shell	N	R (Å)	$\Delta\sigma^2$ (Å ²)	ΔE_0 (eV)	ε_V^2	k^1 -variances (%)	
							Im.	Abs.
Pt L_3 ^{b,d}	Pt–Pt	2.2	2.65	0.00593	9.7	2.5	0.55	0.23
	Pt–Fe	0.9	2.57	0.00858	0.7			
	Pt–C	0.2	1.88	–0.00919	1.5			
	Pt–O*	0.4	3.00	–0.00129	–0.4			
Fe K ^{c,d}	Fe–Pt	2.0	2.57	0.00884	6.7	2.5	0.40	0.20
	Fe–C	3.1	1.79	0.00982	6.0			
	Fe–O*	3.0	2.97	0.00598	–14.5			
	Fe–O _{support}	0.5	2.06	0.00199	–2.0			

^a Notation: N , coordination number; R , distance between absorber and backscatterer atoms; $\Delta\sigma^2$, Debye–Waller factor relative to the Debye–Waller factor of the reference compound; ΔE_0 , inner potential correction accounts for the difference in the inner potential between the sample and the reference compound; ε_V^2 , goodness of fit; the superscript * refers to oxygen from the carbonyl ligands; standard deviations in fits: $N \pm 20\%$, $R \pm 1\%$, $\Delta\sigma^2 \pm 5\%$, $\Delta E_0 \pm 10\%$.

^b R -space fit: $\Delta k = 3.5\text{--}13.5 \text{ \AA}^{-1}$, $\Delta r = 0.5\text{--}4.0 \text{ \AA}$.

^c R -space fit: $\Delta k = 3.5\text{--}15.0 \text{ \AA}^{-1}$, $\Delta r = 0.5\text{--}3.5 \text{ \AA}$.

^d The statistically justified number of free parameters for the Pt and Fe edge fits was found to be 23.

tained by subtracting the pre-edge background from the raw data with a modified Victoreen equation and then dividing the absorption intensity by the height of the absorption edge. The band structure curves were numerically integrated using the XDAP software [17].

2.10. Characterization of bimetallic contributions by EXAFS

The EXAFS such analysis must include data collected at the absorption edge of each metal present, to establish the presence of bimetallic interactions [27]. Moreover, to be reliable and internally consistent, a fit of the EXAFS data at both edges must satisfy certain constraints if bimetallic interactions are present. More specifically, the bimetallic contributions determined at each absorption edge must have the same bond dis-

tances and Debye–Waller factors, with corresponding coordination numbers ($N_{M-M'}$ and $N_{M'-M}$) related to the total number of atoms of each metal (n_M and $n_{M'}$) by the following equation: $N_{M-M'}/N_{M'-M} = n_{M'}/n_M$ [27]. Therefore, if bimetallic interactions are present in the PtFe samples used in this investigation, then the values of $N_{\text{Pt-Fe}}$ and $N_{\text{Fe-Pt}}$ determined from the Pt L_3 and Fe K edges must be related to each other by the following equation:

$$N_{\text{Pt-Fe}}/N_{\text{Fe-Pt}} = n_{\text{Fe}}/n_{\text{Pt}},$$

where n_{Fe} and n_{Pt} are the total numbers of Fe and Pt atoms in the sample, respectively. Because the ratio of $n_{\text{Fe}}/n_{\text{Pt}}$ calculated for these samples on the basis of the precursor stoichiometry and the chemical composition (i.e., approximately 1.0 wt% Pt and 0.11 wt% Fe) is approximately 0.4, the values of $N_{\text{Pt-Fe}}$

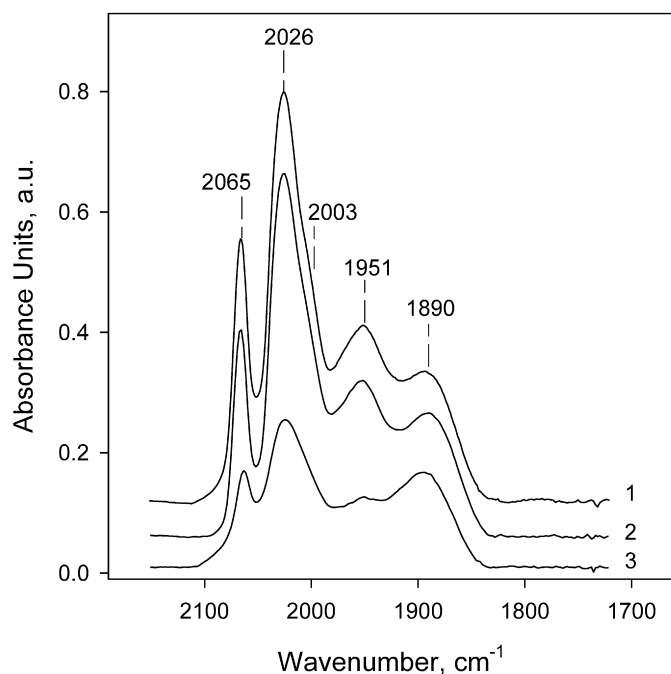


Fig. 3. FTIR spectra in the ν_{CO} region of a freshly prepared $\text{Pt}_5\text{Fe}_2(\text{COD})_2(\text{CO})_{12}/\text{SiO}_2$ sample (1) and of the same sample aged under He flow at room temperature for 24 h (2) and 5 days (3).

and $N_{\text{Fe-Pt}}$ are not expected to be equal to each other, but rather to satisfy the following equation:

$$N_{\text{Pt-Fe}}/N_{\text{Fe-Pt}} = 0.4.$$

3. Results and discussion

3.1. Interaction of $\text{Pt}_5\text{Fe}_2(\text{COD})_2(\text{CO})_{12}$ with SiO_2

We recently reported on the deposition of $\text{Pt}_5\text{Fe}_2(\text{COD})_2(\text{CO})_{12}$ on SiO_2 [12]. Extraction experiments performed with a freshly prepared sample confirmed that this cluster can be completely extracted from the silica surface and that the extracted species have an FTIR “fingerprint” matching that of the original cluster. These results indicate that initial interactions between this cluster and the support are relatively weak and do not involve any reactions between the carbonyl ligands of the cluster and the functional groups of the support [12]. These results are also consistent with literature reports indicating the low reactivity of the silanol groups toward $\text{Fe}_3(\text{CO})_{12}$ and $\text{Fe}(\text{CO})_5$ carbonyl clusters [28]. The adsorption of such clusters on silica is also a reversible process regardless of the pretreatment temperature of the support [28]. Therefore, the set of bands at 2065, 2026, 2003, 1951, and 1890 cm^{-1} observed in the ν_{CO} region of the $\text{Pt}_5\text{Fe}_2(\text{COD})_2(\text{CO})_{12}/\text{SiO}_2$ material represents a unique signature of this cluster on the silica surface (Fig. 3, spectrum 1).

When the $\text{Pt}_5\text{Fe}_2(\text{COD})_2(\text{CO})_{12}/\text{SiO}_2$ sample was aged in He flow at room temperature for 24 h, the intensities of the carbonyl bands remained largely unchanged (Fig. 3, spectrum 2). But longer aging in He flow led to a substantial decrease in the

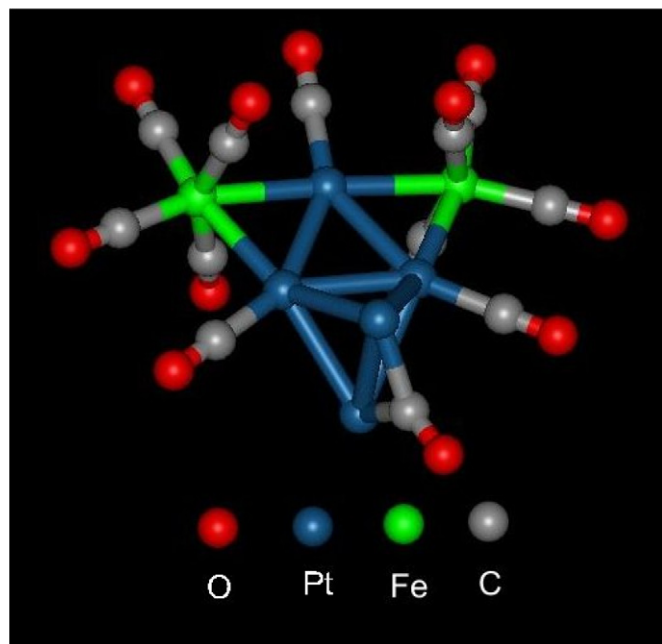


Fig. 4. Structure of crystalline $\text{Pt}_5\text{Fe}_2(\text{COD})_2(\text{CO})_{12}$ drawn based on the XRD data [10]. The COD ligands were omitted for clarity.

Table 3
XRD data characterizing crystalline $\text{Pt}_5\text{Fe}_2(\text{COD})_2(\text{CO})_{12}$ ^a

Shell	<i>N</i>	<i>R</i> (Å)
Pt–Pt	3.2	2.64–2.95 (average), 2.77
Pt–Fe	0.8	2.55–2.60 (average), 2.58
Pt–C*	1.0	1.90
Pt–O*	1.0	3.05
Pt–C	1.6	2.29
Fe–Fe	–	–
Fe–Pt	2.0	2.58
Fe–C*	4.0	1.78
Fe–O*	4.0	2.93

^a Notation: *R*, interatomic distance; *N*, coordination number; C* and O* represent carbon and oxygen atoms of carbonyl ligands, respectively.

intensities of these bands, indicating a slow loss of carbonyl ligands from the supported species (Fig. 3, spectrum 3).

To determine whether the observed loss of carbonyl ligands led to any structural changes, the aged $\text{Pt}_5\text{Fe}_2(\text{COD})_2(\text{CO})_{12}/\text{SiO}_2$ sample also was examined by EXAFS at both the Pt L_3 and Fe K edges; the data are given in Table 2. For comparison, the molecular structure as determined previously by single-crystal X-ray diffraction for the $\text{Pt}_5\text{Fe}_2(\text{COD})_2(\text{CO})_{12}$ precursor is shown in Fig. 4, and its intramolecular bond distances are given in Table 3 [11].

The XRD data characterizing the crystalline $\text{Pt}_5\text{Fe}_2(\text{COD})_2(\text{CO})_{12}$ indicate that the cluster core comprises 5 Pt atoms bonded to one another at an average distance of 2.77 Å, three of which are also bonded to two Fe atoms at an average distance of 2.58 Å (Fig. 4 and Table 3). The cluster core is stabilized by 12 CO ligands, eight of which are bonded to Fe atoms with average Fe–C and Fe–O* distances (where O* is the carbonyl oxygen) of 1.78 and 2.93 Å, respectively. The remaining CO ligands are bonded to Pt atoms with average Pt–C and Pt–O*

distances of 1.90 and 3.05 Å, respectively. In addition, two Pt atoms from the cluster core are connected to two cyclooctadiene ligands at an average Pt–C distance of 2.29 Å.

The Pt L_3 edge EXAFS data (Table 2) characterizing the surface species present in the $\text{Pt}_5\text{Fe}_2(\text{COD})_2(\text{CO})_{12}/\text{SiO}_2$ sample after aging in He for 5 days, indicate that each Pt atom is in close proximity to at least two Pt atoms and 0.9 Fe atom, at average distances of 2.65 and 2.57 Å, respectively. Pt–C and Pt–O* contributions, indicating the presence of carbonyl ligands in the supported species, were also observed with average coordination numbers of 0.2 and 0.4 at average distances of 1.88 and 3.00 Å, respectively. The EXAFS data obtained from the Fe K edge complement those collected at the Pt L_3 edge and indicate the presence of approximately two Pt atoms in the neighborhood of each Fe atom at an average distance of 2.57 Å and approximately three carbonyl ligands, as evidenced by the presence of Fe–C and Fe–O* contributions with average coordination numbers of 3.0 at average distances of 1.79 and 3.0, respectively.

The EXAFS data characterizing the species present in the aged sample clearly show some differences with the XRD data representing crystalline $\text{Pt}_5\text{Fe}_2(\text{COD})_2(\text{CO})_{12}$. Because the sample was kept under an inert atmosphere, and thus the possibility of oxidation can be excluded, the absence of Pt–C contributions from COD ligands and the decreased number of carbonyl ligands attached to both the Pt and Fe atoms in the surface species suggest that the initially weak cluster–support interactions observed during the impregnation step [12] grew stronger with time. This result is not surprising, because it was previously shown that different π - and σ -bonded organic ligands in various organometallic compounds are capable of interacting with surface hydroxyls of silica, with the degree of such interactions depending largely on the nature of the ligand [29]. Moreover, it is also known that carbonyl ligands are capable not only of forming weak hydrogen-bonding interactions with surface hydroxyls, but also of undergoing reactions with the silanol groups according to the following general scheme [28]:



This type of surface reaction has been found to occur in $\text{Ru}_3(\text{CO})_{12}$ and $\text{Os}_3(\text{CO})_{12}$ clusters [30–33]. Our results suggest that a similar process occurs in the $\text{Pt}_5\text{Fe}_2(\text{COD})_2(\text{CO})_{12}$ cluster adsorbed on the surface of silica but at very low rates, leading to the loss of COD and carbonyl ligands only after an extended period.

The observed loss of ligands from the supported cluster had no significant affect on the PtFe bimetallic contributions, because the structural parameters determined from both the Pt L_3 and Fe K edges for Pt–Fe and Fe–Pt contributions remained nearly the same as those characterizing crystalline $\text{Pt}_5\text{Fe}_2(\text{COD})_2(\text{CO})_{12}$ (Tables 2 and 3). Nevertheless, the data in Table 2 indicate that the structure of the cluster core was altered. More specifically, the loss of carbonyl ligands during the aging in He was accompanied by a decrease in the Pt–Pt bond distance from 2.77 to 2.65 Å, which is consistent with literature data demonstrating that the removal of carbonyl ligands

from various supported carbonyl clusters typically leads to a contraction of the metal–metal bonds [34]. Such changes in the metal–metal bond distances usually are attributed to the role of the support, because the loss of CO ligands from the clusters is compensated for by metal–support interactions, with the support becoming a part of the metal ligand shell in partially decarbonylated species [35]. Indeed, the EXAFS data obtained for the aged $\text{Pt}_5\text{Fe}_2(\text{COD})_2(\text{CO})_{12}/\text{SiO}_2$ sample at the Fe K edge also indicated the presence of Fe–O_{support} contributions with an average coordination number of 0.5 at an average distance of 2.06 Å (Table 2). These results suggest that the surface species attach to the silica surface during the loss of carbonyl ligands through Fe atoms rather than Pt atoms, because no Pt–O_{support} contributions were observed. Finally, the average Pt–Pt coordination number observed for the supported species was found to be approximately 2.2 (Table 2), in contrast to the value of 3.2 calculated for crystalline $\text{Pt}_5\text{Fe}_2(\text{COD})_2(\text{CO})_{12}$, suggesting that partial disintegration of the cluster core occurred during the aging. The degree of such disintegration was relatively small, and the PtFe bimetallic interactions were not significantly affected by this process.

3.2. Ligand removal

In previous work, we showed that thermal treatment of a freshly prepared $\text{Pt}_5\text{Fe}_2(\text{COD})_2(\text{CO})_{12}/\text{SiO}_2$ sample in H_2 led to complete decarbonylation of the surface species at approximately 350 °C [12]. Very similar results were obtained when He was substituted for H_2 in the decarbonylation step. The FTIR spectra collected at various temperatures during this process are shown in Fig. 5. The thermal treatment in He flow at 25–50 °C had no significant affect on the intensity of the characteristic bands in the ν_{CO} region at 2065(s),

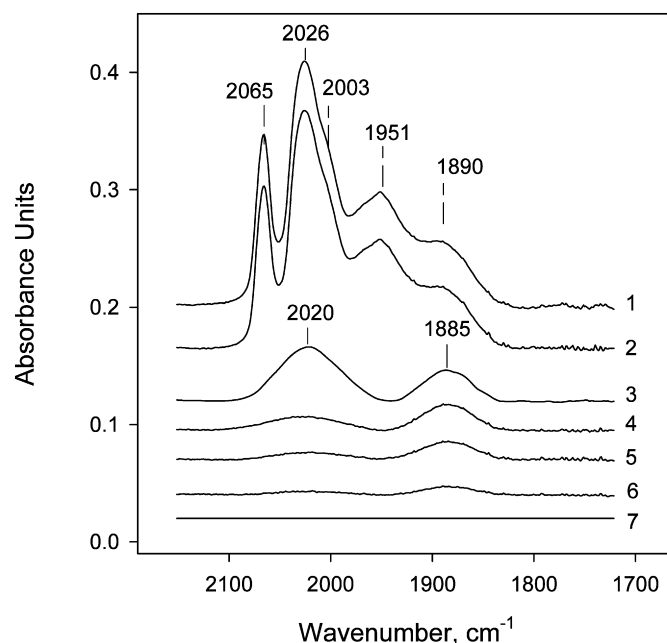


Fig. 5. FTIR spectra in the ν_{CO} region collected during the decarbonylation of $\text{Pt}_5\text{Fe}_2(\text{COD})_2(\text{CO})_{12}/\text{SiO}_2$ in He at (1) 25 °C, (2) 50 °C, (3) 100 °C, (4) 150 °C, (5) 200 °C, (6) 250 °C, and (7) 350 °C.

2026(s), 2003(sh), 1951(m), and 1890(w) cm^{-1} (Fig. 5, spectra 1 and 2), previously assigned to the carbonyl ligands of the SiO_2 -supported $\text{Pt}_5\text{Fe}_2(\text{COD})_2(\text{CO})_{12}$ species [12]. However, substantial changes in the spectra were observed when the temperature was further increased to 100 °C. When a steady state was reached at this temperature after approximately 60 min, the bands at 2065, 2003, and 1951 cm^{-1} were no longer present in the spectrum, whereas the bands at 2026 and 1890 cm^{-1} exhibited a significant decrease in intensity and shifted to 2020 and 1885 cm^{-1} , respectively (Fig. 5, spectrum 3). The analysis of the area under these remaining bands indicates that approximately 70% of the CO ligands were removed from the cluster at this temperature. The bands at 2020 and 1885 cm^{-1} are nearly the same as those observed during the treatment of this sample in H_2 at 100 °C [12], indicating that similar species were formed on the SiO_2 surface at this decarbonylation temperature regardless of the gas used for the treatment. But when the temperature was further increased gradually to 350 °C, the bands at 2020 and 1885 cm^{-1} decreased in intensity and disappeared more rapidly in He than was observed previously in H_2 [12], suggesting that the decomposition of these species follows different pathways in He and H_2 .

Because the decarbonylation chemistry for supported carbonyls is largely unknown, we attempted to gain further insight into this process by monitoring the evolution of CO as a function of temperature from a freshly prepared $\text{Pt}_5\text{Fe}_2(\text{COD})_2(\text{CO})_{12}/\text{SiO}_2$ sample. The CO profile obtained from such a sample during temperature-controlled decarbonylation in H_2 consists of a strong peak with a shoulder located at the low-temperature side; this profile can be modeled with 2 peaks centered at approximately 120 and 144 °C (Fig. 6A). Analysis of the area under these peaks indicates that approximately 80% more CO was desorbed in the high-temperature region than in the low-temperature region (Table 4). The presence of two peaks in the TPD profiles is consistent with the evolution of two types of CO ligands with different M–CO bond strengths and thus different thermal stability. Only 4 of the 12 CO ligands in the original $\text{Pt}_5\text{Fe}_2(\text{COD})_2(\text{CO})_{12}$ cluster are coordinated to Pt; the other 8 CO ligands are coordinated to Fe, yielding a 2:1 ratio for the number of CO molecules released by Fe compared with the number released by Pt. Comparing this value with the 1.8 ratio of the areas of the high- and low-temperature peaks suggests that the low- and high-temperature peaks observed in the TPD profile under H_2 flow can be tentatively assigned to the removal of CO from Pt and Fe, respectively.

Literature data indicate that in various carbonyl clusters, the M–CO bond dissociation energy varies with the CO/M ratio, with carbonyl ligands binding more strongly to the metal in clusters with multiple CO ligands [36]. In the case of the $\text{Pt}_5\text{Fe}_2(\text{COD})_2(\text{CO})_{12}$ cluster, these results suggest that CO ligands coordinated to Pt should be released first during the thermal treatment. Moreover, a general assumption that shorter bonds are stronger has been found to be true for various chemical compounds with covalent bonds, as indicated by the available structural and thermochemical data [36]. Finally, literature data indicate that experimentally and theoretically determined dissociation energies for the Fe–CO bonds in various $\text{Fe}_x(\text{CO})_y$ carbonyl clusters range from 28 to 32 kcal mol^{-1} , whereas corresponding values for Pt–CO bonds in $\text{Pt}_x(\text{CO})_y$ clusters are approximately 10 kcal mol^{-1} [37,38].

In a similar TPD experiment performed in the presence of He, the CO profile once again was found to comprise two peaks centered at 110 and 140 °C (Fig. 6B). These two peaks also can be assigned to the evolution of CO from the Pt and Fe atoms of the cluster core, respectively. Directly comparing these peaks with those detected during decarbonylation in H_2 (Fig. 6C)

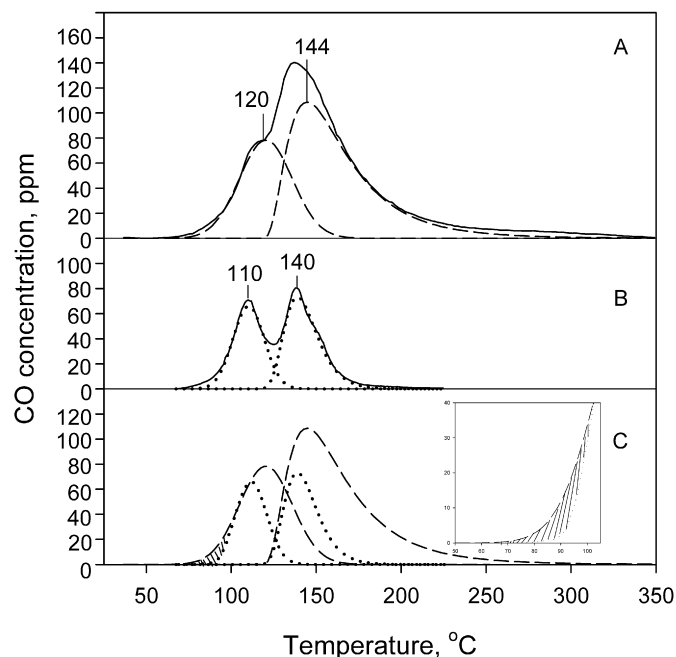


Fig. 6. CO TPD profiles for $\text{Pt}_5\text{Fe}_2(\text{COD})_2(\text{CO})_{12}/\text{SiO}_2$ treated in H_2 (A), or He (B). A direct comparison of the CO desorption peaks during treatment in H_2 (dashed line) and He (dotted line) is shown in (C).

Table 4
TPD results obtained with the $\text{Pt}_5\text{Fe}_2(\text{COD})_2(\text{CO})_{12}/\text{SiO}_2$ catalyst

Treatment conditions	Removal of carbonyl ligands		Results of peak deconvolution			Amount of residual carbon ^a	
	Total CO desorption area (a.u.)	Relative ratio	Peak maximum temperature (°C)	Peak area (a.u.)	Relative ratio	ppm	Relative ratio
H_2 350 °C	8700	2.6	120	3080	1.0	370	1.0
			144	5620	1.8		
He 350 °C	3400	1.0	110	1540	1.0	870	2.4
			140	1860	1.2		

^a Determined by elemental analysis (ICP).

demonstrates some differences between decarbonylation in He and H₂; for example, the difference in the initial slopes observed at 50–100 °C (see insert) indicates that H₂ facilitated the removal of CO from the cluster core at lower temperatures. However, the decarbonylation process stopped more rapidly in He (at 230 °C) than in H₂ (at 350 °C), consistent with our FTIR results discussed above and elsewhere [12].

During decarbonylation in He, the maxima of both desorption peaks appeared at lower temperatures than those observed under the H₂ flow. More specifically, the difference in peak position for the CO species desorbing from Pt was approximately 10 °C, whereas a shift of only 4 °C was observed for the CO species desorbing from Fe (Figs. 6A and 6B). Because the decarbonylation process from both metals likely occurs through stepwise removal of CO ligands, it would be expected that in the presence of H₂, the vacancies formed on metal sites would be occupied by hydrogen. In contrast, the metal sites should remain clean in He. H₂ adsorption on the metal sites would be expected to increase the electron density on both metals, resulting in increased back π -bonding to the remaining CO ligands and thus increased Pt–CO and Fe–CO bond strength. The presence of electronic interactions between Pt and Fe also would be expected to affect this process; for example, the electron density in supported Pt–Fe bimetallics would be shifted to some degree from Fe to Pt, as has been shown for bulk PtFe alloys [39]. Such a shift would result in increased back π -bonding from Pt compared with that from Fe, consistent with the differences in the positions of the CO peaks desorbing from Pt and Fe in He and H₂.

The overall area under the CO peaks observed during ligand removal in He was approximately 2.6 times smaller than that observed during ligand removal in H₂ (Fig. 6C and Table 4), suggesting the release of smaller amounts of carbonyl ligands in the form of CO during He treatment. Thus, along with CO desorption, a side reaction between CO ligands also likely occurred during these treatments. To verify this hypothesis, we analyzed Pt₅Fe₂(COD)₂(CO)₁₂/SiO₂ samples treated in He or H₂ for the presence of any carbon residues. In both cases, we found residual carbon on the catalyst surface (Table 4). However, less carbon was detected in the H₂-treated sample than in the He-treated sample (370 vs 870 ppm, a difference factor of 2.4). This result is consistent with the 2.6 difference factor in the amount of CO released in the gas phase during these processes. Therefore, it appears that COD ligand decomposition is not a major source of residual carbon.

Qualitative results obtained with gas chromatography analysis of the reactor outlet stream during decarbonylation in He indicated the appearance of CO₂ starting at approximately 100 °C. In contrast, no CO₂ was detected during decarbonylation in H₂. No CH₄ formation was detected in either case. As a result, the formation of carbon deposits and the presence of CO₂ in the outlet stream can be rationalized in terms of the Boudouard reaction between two CO molecules,



This reaction is known to be catalyzed by various transition metals, including Pt and Fe [40]. Although its mechanism re-

mains poorly understood, generally it is assumed that dissociation of one CO molecule is required to form atomic oxygen species capable of interacting with CO to form CO₂ [41]. The presence of residual carbon even in the sample decarbonylated in H₂ indicates that the Boudouard reaction may also proceed in this case, but at a lower rate and with CO₂ formation apparently below our detection limit. Quantitative analysis of the TPD results indicates that CO ligands attached to both metals in the cluster core participated in the Boudouard reaction, because the Pt and Fe peaks were equally reduced in magnitude in the CO desorption profile of the He-treated sample (Fig. 6). But the same results suggest that a larger fraction of the CO ligands initially attached to Fe were involved in this reaction. Similar TPD data, indicating that carbonyl groups in Al₂O₃- or ZrO₂-supported NaRuCo₃(CO)₁₂, Ru₃(CO)₁₂, and C₃H₇CCO₃(CO)₉ clusters can disproportionate during decarbonylation, have been reported previously [42]. Our findings further demonstrate that a cleaner catalyst surface can be obtained by using H₂ in the ligand removal step.

3.3. EXAFS characterization

3.3.1. Decarbonylation of Pt₅Fe₂(COD)₂(CO)₁₂ under He

Table 5 summarizes the structural parameters characterizing the surface species formed after the treatment of Pt₅Fe₂(COD)₂(CO)₁₂/SiO₂ in He at 350 °C. The Pt L₃ edge data indicate the presence of only first-shell Pt–Pt contributions with an average coordination number of 3.6 at an average bonding distance of 2.74 Å. Two Pt–O contributions observed at short (Pt–O_s) and long (Pt–O_l) distances of 2.14 and 2.67 Å, respectively, are typical of noble metal interactions with metal oxide supports [34]. The absence of higher Pt–Pt shells and the low value of $N_{\text{Pt–Pt}}$ observed for this sample are consistent with the formation of highly dispersed Pt clusters on the silica surface incorporating on average no more than 6 Pt atoms. These clusters appear to be largely isolated from the Fe atoms, because the spectra demonstrate no evidence of Pt–Fe contributions.

Complementing the Pt L₃ edge data, the structural parameters obtained from the Fe K edge (Table 5) also demonstrate the absence of any Fe–Pt contributions, confirming that Pt and Fe atoms are not in direct contact on the silica surface after the He treatment. The multiple Fe–O contributions detected in the spectra of this sample point to the more complex interactions of the Fe atoms with the support and the formation of oxide-like Fe species. The first and second Fe–O shells have been observed in bulk FeO at 2.15 and 3.73 Å, in Fe₂O₃ at 1.94 and 2.12 Å, and in Fe₃O₄ at 1.89 and 3.49 Å, respectively [43–45]. Because the bond distances for the Fe–O contributions reported in Table 5 do not directly match any of those reported previously for bulk oxides, we can infer that no bulk forms of iron oxide species were formed on the surface of silica under these conditions. This finding could be due in part to the low Fe content of the sample.

In summary, the EXAFS results clearly show that the thermal removal of the ligands from the SiO₂-supported Pt₅Fe₂(COD)₂(CO)₁₂ clusters in He led to the disintegration of the bimetallic cluster frame and the formation of highly dispersed

Table 5

EXAFS parameters characterizing the surface species formed after treatment of Pt₅Fe₂(COD)₂(CO)₁₂/SiO₂ in He at 350 °C. (Notation as in Table 2 with the exceptions noted at the bottom)

Edge	Shell	N	R (Å)	$\Delta\sigma^2$ (Å ²)	ΔE_0 (eV)	ε_V^2	k^1 -variances (%)	
							Im.	Abs.
Pt L_3 ^{a,c}	Pt–Pt	3.6	2.74	0.00482	–5.0	2.7	0.53	0.21
	Pt–O _{support}							
	Pt–O _s ^d	1.7	2.14	0.00737	–7.1			
	Pt–O _l ^d	0.7	2.67	–0.00294	–2.6			
Fe K ^{b,c}	Fe–O _{support}					3.8	0.67	0.33
	Fe–O ₁	2.3	1.99	0.00822	0.5			
	Fe–O ₂	0.9	2.67	0.00252	–17.2			
	Fe–O ₃	2.0	3.29	–0.00065	7.6			

^a R-space fit: $\Delta k = 3.5\text{--}15.0 \text{ \AA}^{-1}$, $\Delta r = 1.0\text{--}3.5 \text{ \AA}$.^b R-space fit: $\Delta k = 3.5\text{--}15.0 \text{ \AA}^{-1}$, $\Delta r = 0.5\text{--}3.5 \text{ \AA}$.^c The statistically justified number of free parameters for the Pt and Fe edge fits was found to be 19 and 23, respectively.^d The subscripts s and l refer to short and long, respectively.

Table 6

EXAFS parameters characterizing the surface species formed after treatment of Pt₅Fe₂(COD)₂(CO)₁₂/SiO₂ in H₂ at 350 °C. (Notation as in Table 2 with the exceptions noted at the bottom)

Edge	Shell	N	R (Å)	$\Delta\sigma^2$ (Å ²)	ΔE_0 (eV)	ε_V^2	k^1 -variances (%)	
							Im.	Abs.
Pt L_3 ^{a,c}	Pt–Pt	6.0	2.74	0.00296	0.9	2.3	1.65	0.48
	Pt–Fe	0.9	2.67	0.00720	–2.0			
	Pt–O _{support}							
	Pt–O _s ^d	0.9	2.13	0.01000	–5.0			
	Pt–O _l ^d	1.4	2.69	–0.00226	–6.8			
Fe K ^{b,c}	Fe–Pt	2.3	2.67	0.00745	4.6	3.0	1.12	0.46
	Fe–O _{support}							
	Fe–O ₁	0.7	1.96	0.01000	–3.2			
	Fe–O ₂	0.3	2.54	–0.00143	0.2			

^a R-space fit: $\Delta k = 3.5\text{--}15.0 \text{ \AA}^{-1}$, $\Delta r = 1.0\text{--}3.5 \text{ \AA}$.^b R-space fit: $\Delta k = 3.5\text{--}15.0 \text{ \AA}^{-1}$, $\Delta r = 1.0\text{--}3.5 \text{ \AA}$.^c The statistically justified number of free parameters for both the Pt and Fe edge fits was found to be 19.^d The subscripts s and l refer to short and long, respectively.

Pt clusters with a nuclearity of six and oxide-like Fe species. However, we cannot exclude the possibility that some of these Fe species may have been located in close proximity to the Pt clusters.

3.3.2. Decarbonylation of Pt₅Fe₂(COD)₂(CO)₁₂ under H₂

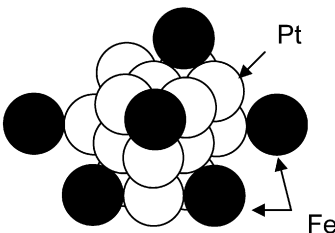
Table 6 summarizes the structural parameters characterizing the surface species formed after the treatment of Pt₅Fe₂(COD)₂(CO)₁₂/SiO₂ in H₂ at 350 °C. The Pt L_3 edge data indicate that the first coordination shell of Pt consisted of approximately 6 Pt atoms and 1 Fe atom at average bonding distances of 2.74 and 2.67 Å, respectively. The EXAFS data collected at the Fe K edge for the same sample supplement the information obtained at the Pt L_3 edge and indicate the presence of approximately 2.3 Pt atoms in the first coordination shell of Fe at an average bond distance of 2.67 Å. These results demonstrate that the Pt–Fe and Fe–Pt contributions determined from the two different edges yielded the same bond distances, and that the corresponding Debye–Waller factors are indistinguishable within experimental uncertainty. Moreover, the calculated $N_{\text{Pt–Fe}}/N_{\text{Fe–Pt}}$ ratio of 0.43 is nearly the same as the Fe atom/Pt atom ratio of 0.40 in

the sample. Thus, the data analysis appears to be internally consistent and reliable [27]. Therefore, the EXAFS data collected at both the Pt L_3 and Fe K edges unambiguously indicate the presence of Pt–Fe bimetallic interactions in this sample after the treatment in H₂. This conclusion is further reinforced by earlier published XEDS data [12] for the same sample showing no evidence of segregation of Pt and Fe into separate particles. In fact, the XEDS data indicate that all metal particles formed on the SiO₂ surface are bimetallic and that most of them have a Pt/Fe atomic ratio of approximately 2.5, consistent with the stoichiometry of the original Pt₅Fe₂(COD)₂(CO)₁₂ cluster [11].

The observed Pt–Pt coordination number of 6 is substantially larger than that found in the original cluster, indicating that the metal particles formed on the silica surface after the treatment in H₂ did not consist of individual Pt₅Fe₂ units. An increase in the Pt–Pt coordination number may indicate cluster disintegration and subsequent aggregation of Pt atoms; however, if this were the case, then the coordination number for the Pt–Fe contributions would also be expected to decrease significantly for both the Pt and Fe edges. Because this is not the case, we can alternatively suggest that the metal particles likely

Table 7

Suggested structural model of bimetallic particles formed on the SiO₂ surface from Pt₅Fe₂(COD)₂(CO)₁₂ after ligand removal in H₂ at 350 °C (interactions between the metals and the support are not included for simplicity)

Proposed structure	Shell	<i>N</i> ^a
	Pt–Pt	5.8
	Pt–Fe	1.1
	Fe–Fe	–
	Fe–Pt	2.5

^a Notation: *N*, calculated coordination number.

are formed as a result of the condensation of several Pt₅Fe₂ units occurring without disintegration of the bimetallic cluster core. As described previously [46,47], average metal coordination numbers can be used to estimate average sizes of metal nanoparticles based on different models that correlate these two parameters [48–50]. The weighted-average metal–metal coordination number, calculated as $N_{M-M} = (5N_{Pt-M} + 2N_{Fe-M})/7$ based on the Pt/Fe atomic ratio, was found to be approximately 5.6 for the sample treated in H₂, implying an average size of 1 nm. This value suggests that the individual particles formed incorporate no more than 30 metal atoms, nearly 94% of which are exposed on the surface. These results correlate well with high-resolution transmission electron microscopy (HRTEM) data reported previously for this sample [12]. Based on these estimates, we can suggest that the removal of ligands in H₂ led to the condensation of approximately 3 cluster units, and that the resulting supported particles consisted of an average of approximately 15 Pt atoms and 6 Fe atoms closely packed together. A graphical illustration of a possible model to describe these particles is shown in Table 7. The metal–metal coordination numbers calculated from this model are in a good agreement with our experimental data. We also note that both the Pt and Fe atoms in such particles interacted with the support to a similar extent, as demonstrated by the presence of both Pt–O_{support} and Fe–O_{support} contributions in the spectra (Table 6).

Table 8

EXAFS parameters characterizing the surface species formed after treatment of PtFe/SiO₂ in H₂ at 350 °C. (Notation as in Table 2 with the exceptions noted at the bottom)

Edge	Shell	<i>N</i>	<i>R</i> (Å)	$\Delta\sigma^2$ (Å ²)	ΔE_0 (eV)	ε_{γ}^2	<i>k</i> ¹ -variances (%)	
							Im.	Abs.
Pt <i>L</i> ₃ ^{a,b}	Pt–Pt	7.7	2.74	0.00638	–6.1	3.7	0.95	0.47
	Pt–Fe	1.0	2.68	0.00464	–8.8			
	Pt–O _{support}							
	Pt–O _s ^c	0.7	2.04	0.01000	–2.2			
Fe <i>K</i> ^{a,b}	Fe–Pt	2.6	2.68	0.00417	6.0	2.7	1.98	1.27
	Fe–Fe	0.3	2.85	–0.00299	–2.4			
	Fe–O _{support}							
	Fe–O _s ^c	1.4	2.07	0.01000	0.2			

^a *R*-space fit: $\Delta k = 3.5\text{--}15.0 \text{ \AA}^{-1}$, $\Delta r = 1.0\text{--}4.0 \text{ \AA}$.

^b The statistically justified number of free parameters for both the Pt and Fe edge fits was found to be 23.

^c The subscript s refer to short.

In summary, we found that the choice of the thermal treatment used to remove the ligands from SiO₂-supported Pt₅Fe₂(COD)₂(CO)₁₂ clusters had a significant effect on the structure of the resulting metal particles. Treatment in He led to complete disintegration of the PtFe bimetallic cluster core and the subsequent formation of small Pt clusters and Fe oxide-like species, whereas treatment in H₂ resulted in the formation of PtFe bimetallic particles with an average size of approximately 1 nm. The formation of such different surface structures allows us to evaluate their catalytic performance and determine their structure–reactivity relationships, as we discuss below.

3.3.3. Structural characterization of PtFe/SiO₂ prepared by coimpregnation

The data collected at the Pt *L*₃ edge for the PtFe/SiO₂ sample prepared by co-impregnation of individual Pt and Fe precursors and treated in H₂ at 350 °C reveal approximately 8 Pt atoms and 1 Fe atom in the first coordination shell of Pt at average distances of 2.74 and 2.68 Å, respectively (Table 8). Supplemental structural information obtained for the same sample from the analysis of the Fe *K* edge data confirm the Fe–Pt bimetallic interactions, as indicated by the presence of the Fe–Pt contributions with an average coordination number of 2.6 at a distance of 2.68 Å. The data collected at the two edges are internally consistent according to the aforementioned criteria. The presence of the Pt–Fe contributions demonstrates that PtFe bimetallic species can also be formed on the SiO₂ surface by co-impregnation of individual Pt and Fe precursors, followed by a reduction step in H₂ at elevated temperatures. However, in this case the calculated fraction of bimetallic contributions for each investigated absorption edge was approximately 30% lower than that in the sample prepared from the Pt₅Fe₂(COD)₂(CO)₁₂ precursor (Table 9). These results are consistent with those of XEDS analysis performed on individual particles, which demonstrated the presence of both Pt and Fe in only some of these particles, with an average composition of 85% Pt and 15% Fe on an atomic basis [12]. Moreover, some of the metal particles were found to be monometallic in nature, suggesting that some fraction of both metals remained segregated [12]. The Fe–Fe contributions observed in this sample, with an average coordination number of

Table 9
White line area and estimated fraction of bimetallic contributions for various SiO₂-supported samples

Sample	Preparation technique	Treatment conditions	White line area ^a	Fraction of bimetallic interactions	
				$N_{\text{Pt-Fe}}/(N_{\text{Pt-Fe}} + N_{\text{Pt-Pt}})$	$N_{\text{Fe-Pt}}/(N_{\text{Fe-Pt}} + N_{\text{Fe-Fe}})$
Pt ₅ Fe ₂ /SiO ₂	Impregnation of Pt ₅ Fe ₂ (COD) ₂ (CO) ₁₂	H ₂ 350 °C	4.54	0.13	1.00
PtFe/SiO ₂	Co-impregnation of H ₂ PtCl ₆ and Fe(NO ₃) ₃	H ₂ 350 °C	4.68	0.10	0.70
Pt/SiO ₂	Impregnation of H ₂ PtCl ₆	H ₂ 350 °C	5.23	–	–

^a Determined from XANES data collected at the Pt L₃ edge.

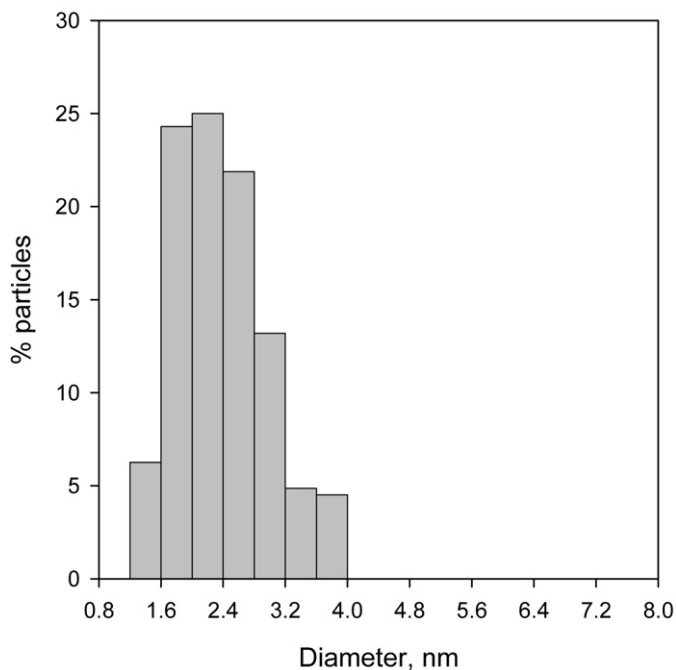


Fig. 7. Metal particle size distribution obtained from HRTEM images of PtFe/SiO₂ reduced in H₂ at 350 °C [12].

0.3 at an average distance of 2.85 Å, likely represent Fe–O–Fe bridges and not closely packed Fe–Fe units, because the distance was substantially longer than that typically observed for Fe foil [51].

The overall weighted average metal–metal coordination number calculated for this sample was found to be approximately 7.0, indicating that this sample was less dispersed than the cluster-derived sample of similar composition. The particle size distribution determined from HRTEM images of PtFe/SiO₂ reduced in H₂ at 350 °C is shown in Fig. 7 [12]. The metal particles ranged in size from 1.0 to 4.0 nm (average, ca. 2.6 nm), indicating a metal dispersion of ca. 43%.

3.4. Chemisorptive properties

3.4.1. H₂ chemisorption

Table 10 summarizes hydrogen chemisorption data for different Pt and PtFe samples reduced in H₂ at 350 °C. The H/Pt ratio determined for the monometallic Pt/SiO₂ sample was in good agreement with the dispersion of Pt estimated from HRTEM data, indicating that both techniques can be used re-

Table 10
Hydrogen chemisorption and metal dispersion for various catalysts reduced in H₂ at 350 °C

Sample	Treatment	H/Pt ^a	Pt _s /Pt _t ^b	ϕ _H ^c
Pt/SiO ₂	H ₂ 350 °C	0.50	0.45 ^c	1.00
PtFe/SiO ₂	H ₂ 350 °C	0.29	0.43 ^c	0.67
Pt ₅ Fe ₂ /SiO ₂	H ₂ 350 °C	0.41	0.94 ^d	0.44

^a Hydrogen chemisorption at 25 °C determined with respect to total number of Pt atoms in the sample.

^b Dispersion (i.e., fraction of Pt atoms exposed at the surface).

^c Determined from HRTEM data.

^d Estimated from EXAFS data using the model of Kip et al. [48].

^e Fraction of surface Pt atoms covered by hydrogen.

liably for the dispersion estimates when the composition of the sample is simple. As expected, a control experiment with a Fe/SiO₂ sample yielded no strong hydrogen chemisorption on Fe under our experimental conditions. In agreement, previous theoretical calculations performed for a FePd system also indicated that hydrogen is bonded mainly to Pd atoms [52]. Therefore, in the analysis of the chemisorption data for the PtFe bimetallic samples, H/Pt atomic ratios were calculated considering only the total number of Pt atoms in the sample. The data given in Table 10 reveal significantly lower H/Pt ratios for the PtFe/SiO₂ and Pt₅Fe₂/SiO₂ samples than might be expected based on the metal dispersions, thus suggesting alteration of the chemisorptive properties of Pt in the presence of Fe. Considering both sets of data, it appears that the coverage of platinum by hydrogen in PtFe/SiO₂ and Pt₅Fe₂/SiO₂ was approximately 67 and 44%, respectively.

This finding is consistent with previous literature reports suggesting a reduction in the hydrogen chemisorptive capacity of Pt in PtFe bimetallic species on various supports [53,54]. Moreover, these same literature reports suggested a dependence of hydrogen chemisorption on iron content due to the tendency of Fe to preferentially enrich the surface of bimetallic PtFe particles, thus blocking hydrogen adsorption on Pt sites. But our EXAFS data for both the PtFe/SiO₂ and Pt₅Fe₂/SiO₂ samples provide no clear evidence for the presence of Fe on the Pt surface. Moreover, our structural data clearly indicate that Pt and Fe interacted with the support to a fairly similar degree, based on the number of oxygen neighbors present in the coordination shell of each metal. Therefore, it appears that possible coverage of Pt by Fe atoms was not the primary reason for the reduced hydrogen chemisorption capacity; instead, our chemisorption and structural data suggest that the affect of Fe

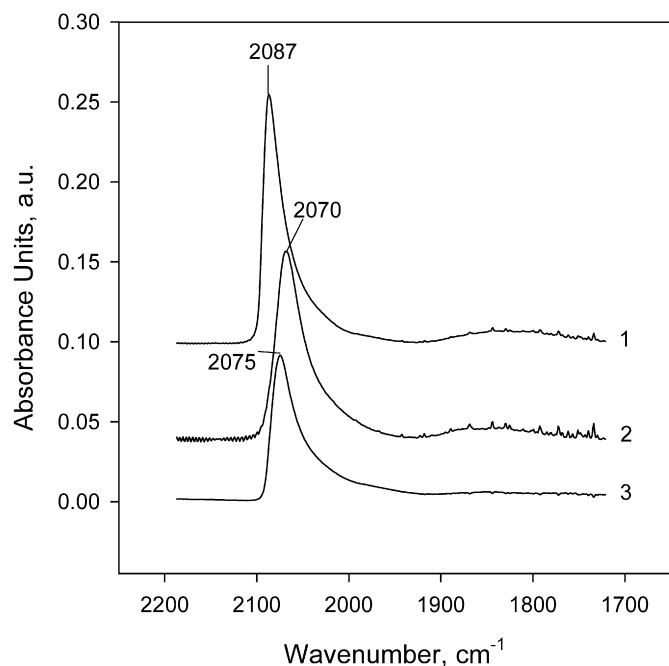


Fig. 8. FTIR spectra of CO (75 Torr) adsorbed at room temperature on (1) 1% Pt/SiO₂, (2) Pt₅Fe₂/SiO₂, and (3) PtFe/SiO₂ pretreated in H₂ at 350 °C.

on the chemisorptive properties of platinum was maximized in the cluster-derived Pt₅Fe₂/SiO₂ sample, which exhibited a larger fraction of bimetallic Pt–Fe interactions. Thus, we can suggest that these Pt–Fe interactions were primarily responsible for altering the chemisorptive properties of platinum.

3.4.2. CO adsorption

Fig. 8 shows FTIR spectra of CO adsorbed on Pt/SiO₂, PtFe/SiO₂, and Pt₅Fe₂/SiO₂. When these samples were reduced in H₂ at 350 °C and exposed to 75 Torr of CO at room temperature, two bands were observed in the ν_{CO} region of the spectra of all samples at 2087–2070(s) and approximately 1850(w) cm⁻¹. These bands can be assigned to terminal and bridging CO species, respectively, adsorbed on reduced Pt sites [55]. CO adsorbed on reduced Fe sites would be expected to appear at approximately 2040 cm⁻¹ [56]; however, the bands corresponding to the Fe–CO species likely were of very low intensity under our experimental conditions, and thus, were covered by the low wavenumber tailing of the strong bands of the terminal CO species adsorbed on Pt sites. Compared with the terminal Pt–CO band for the Pt/SiO₂ sample, the bands corresponding to the same species were shifted toward lower frequencies by approximately 12 cm⁻¹ for the PtFe/SiO₂ sample and 17 cm⁻¹ for the Pt₅Fe₂/SiO₂ sample. The vibrational frequency of CO adsorbed on noble metals can be influenced by the electronic state of the metal sites and/or the degree of CO dipole–dipole coupling. The extent of such coupling is affected by CO coverage, and under saturation conditions, by the size of the active metal ensemble. Whereas on monometallic catalysts, the ensemble size is equivalent to the metal particle size [57, 58], in bimetallic systems, surface dilution by the second metal may lead to different active metal ensemble sizes despite a similar overall metal particle size, as we reported previously for

the Pt–Au system [59]. Thus, in this current work, even though the Pt/SiO₂ and PtFe/SiO₂ samples have nearly the same metal dispersion and metal particle size (Table 10), we cannot exclude the possibility that the Pt ensemble sizes are different and, therefore, coupling effects may also contribute to the observed differences in the terminal Pt–CO stretching vibrational frequency. Additional information obtained from XANES results suggests that electronic effects may be the primary cause of these differences, however, as we discuss next.

According to the Blyholder model [57], a red shift indicates the adsorption of CO on electron-rich Pt sites due to an increased back-donation of electrons from the filled Pt *d* orbitals to the 2 π^* orbitals of the CO molecule. Indeed, analysis of the XANES regions of the XAFS spectra of the different samples (Table 9) supports such an explanation. More specifically, in the XANES spectra, the observed band structure for the Pt *L*₃ edge, commonly called the “white line,” is indicative of the absorption threshold resonances associated with the likelihood of excitations of 2*p*_{3/2} electrons to unoccupied *d* states [27]. It is generally assumed that the white line correlates with the electron density of metal atoms, with a decrease in the white line area indicating a decrease in the electron density of these atoms [27,60]. The results given in Table 9 indicate that both bimetallic samples had smaller white line areas than Pt/SiO₂, with the effect maximized for the Pt₅Fe₂/SiO₂ sample. Such a reduced white line area suggests the presence of strong electronic interactions between Pt and Fe in the bimetallic samples. Therefore, consistent with our XANES and structural data, the presence of a shift in the vibrational frequency of terminally adsorbed CO in the FTIR spectra of both the PtFe/SiO₂ and Pt₅Fe₂/SiO₂ samples can be attributed primarily to an electronic modification of Pt sites by Fe due to the presence of Pt–Fe interactions on the surface of both catalysts. The extent of this shift was greater for the Pt₅Fe₂/SiO₂ sample (i.e., 17 cm⁻¹), as would be expected considering the larger fraction of bimetallic interactions in this sample (Table 9).

Once the adsorption of CO reached a steady state in each sample, the stability of the adsorbed CO species at room temperature was evaluated by flushing the gas-phase CO with He and monitoring the intensities of the terminal CO bands versus time. These results are summarized in Fig. 9. The slopes of the curves obtained are proportional to the desorption rates and indicate higher rates of CO desorption from PtFe/SiO₂ and Pt₅Fe₂/SiO₂ as compared to Pt/SiO₂, suggesting relatively weaker bonding of CO to the surface of the bimetallic PtFe samples. This conclusion contradicts what would be expected based on the interaction of CO with metals according to the Blyholder model, which suggests that an increased electron density on the CO 2 π^* molecular orbital results in a weakening of the C≡O bond and thus a simultaneous strengthening of the Pt–C bond [57]. But previous studies showed that an increase in the electron density on a noble metal site due to the electronic influence of a promoter did not necessarily lead to an increase in the strength of the M–C bonds [61,62]; in fact, the binding energy of CO was found to be lower on bimetallic surfaces (i.e., PtSn, PtFe) than on the corresponding monometallic surfaces [63,64]. These experimental results agree with theoretical calculations

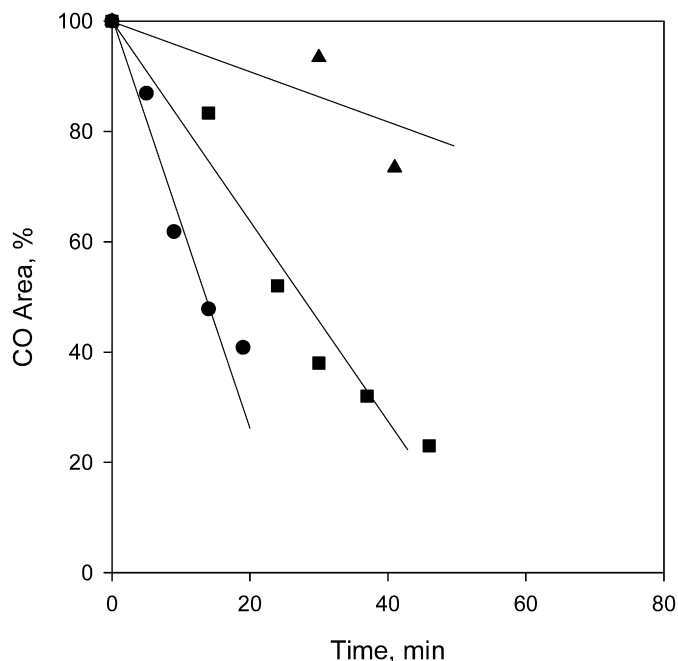


Fig. 9. CO desorption curves obtained from FTIR data at 25 °C for Pt/SiO₂ (▲), Pt₅Fe₂/SiO₂ (●), and PtFe/SiO₂ (■) pretreated in H₂ at 350 °C.

showing an increased electron density of the Pt atoms adsorbing CO and an elongated Pt–C bond upon alloying [61,62].

Overall, our FTIR experimental data (Fig. 9) indicate that the weakest CO adsorption was found on the Pt₅Fe₂/SiO₂ sample, as manifested by the largest shift of the ν_{CO} band to lower frequencies and the fastest rate of CO desorption. This sample also exhibited the largest fraction of Pt–Fe bimetallic interactions. Therefore, it appears that the strength of CO adsorption on the PtFe bimetallic surfaces is directly related to the degree of atomic mixing of the two metals, and thus, also to the extent of the electronic modification of Pt caused by Fe.

3.4.3. NO adsorption

The similar distribution of electrons in CO and NO allows the use of both molecules to probe metal surfaces. Because NO has an extra electron occupying the π^* antibonding molecular orbital, however it can be more sensitive to the electronic state of the adsorbate; in this orbital, even slight changes in the electron density noticeably change the frequency of the ν_{NO} vibrations [65]. Therefore, the general behavior of NO during the adsorption on metal surfaces and the formation of M–NO bonds can be interpreted using the same arguments as proposed for the adsorption of CO [65]. Furthermore, using NO to probe the surface of PtFe bimetallic catalysts provides additional information regarding the oxidation state of Fe. However, NO adsorption experiments can become rather complex, because both metals are capable of interacting with NO, and IR bands corresponding to the Pt–NO and Fe–NO species overlap. We have established experimentally that CO and NO exhibit different adsorption strengths on these metals; for example, NO binds weakly on Pt sites, and a large fraction of adsorbed NO species can be displaced from the Pt sites during subsequent exposure to CO, which exhibits significantly stronger adsorption

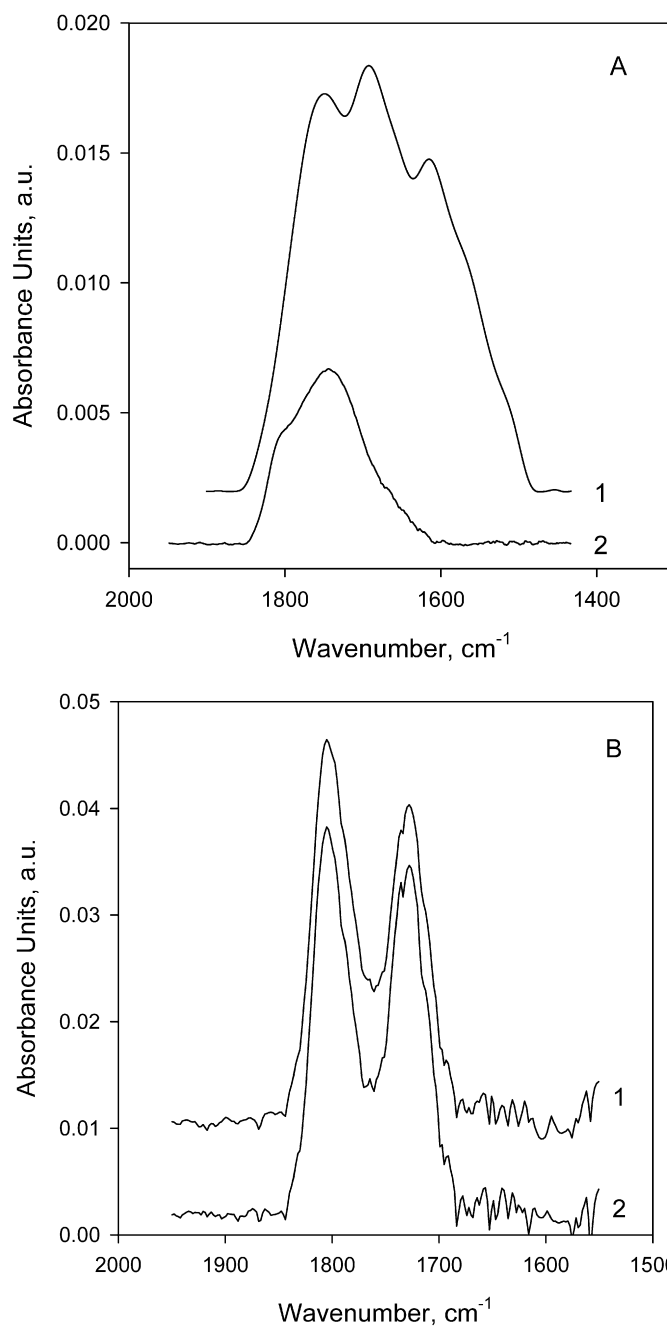


Fig. 10. FTIR spectra in the ν_{NO} region collected after exposure of (A) Pt/SiO₂ and (B) Fe/SiO₂ pretreated in H₂ at 350 °C to: (1) 75 Torr NO for 5 min at room temperature and subsequent purging with He to remove NO from the gas phase, and (2) additional exposure of the NO-treated samples to 75 Torr of CO for 5 min, and subsequent purging with He to remove CO from the gas phase.

(Fig. 10A). In contrast, CO adsorption on Fe is relatively weak; therefore, any surface Fe–NO species formed during exposure to NO are not significantly affected by subsequent exposure to CO (Fig. 10B). Consequently, we used consecutive exposures to NO and CO in our FTIR experiments in an attempt to differentiate the Fe–NO bands from the Pt–NO bands; Fig. 11 shows the results of these experiments.

The spectrum of the Pt/SiO₂ sample collected after consecutive exposure to 75 Torr of NO at room temperature for 5 min, purging with He, and subsequent exposure to 75 Torr

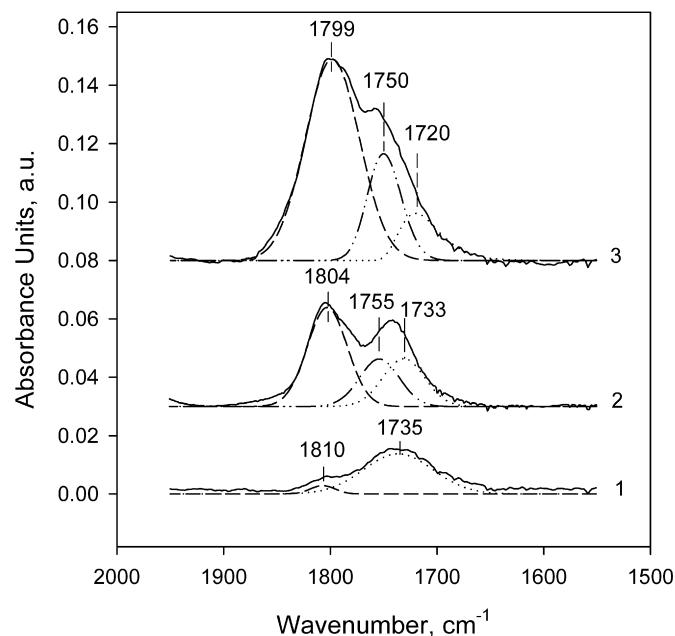


Fig. 11. FTIR spectra in the ν_{NO} region collected after exposure of (1) Pt/SiO₂, (2) PtFe/SiO₂, and (3) Pt₅Fe₂/SiO₂ pretreated in H₂ at 350 °C to 75 Torr NO for 5 min at room temperature, purging with He, exposure to 75 Torr of CO for 5 min, and subsequent purging with He to remove CO from the gas phase.

of CO for 5 min included two bands at 1810 and 1735 cm⁻¹ after the removal of CO from the gas phase. These bands can be assigned to nitrosyl species remaining on the Pt surface in straight and bent configurations, respectively (Fig. 11, spectrum 1) [55]. A more complex spectrum was observed in the case of PtFe/SiO₂, the deconvolution of which revealed the presence of three bands at approximately 1804, 1755, and 1733 cm⁻¹ (Fig. 11, spectrum 2). Three bands were also observed in the spectrum of the Pt₅Fe₂/SiO₂ sample at 1799, 1750, and 1720 cm⁻¹ (Fig. 11, spectrum 3). Comparing the spectra of the bimetallic samples with that of Pt/SiO₂ suggests that the band at 1735–1720 cm⁻¹ can be assigned to NO adsorbed on Pt sites in a bent configuration [55]. The position of this band shifted to lower wavenumbers in the order Pt/SiO₂ > PtFe/SiO₂ > Pt₅Fe₂/SiO₂, similar to what was observed during the adsorption of CO on the same samples. These results once again suggest that the electronic properties of Pt were significantly affected in the bimetallic samples, with the effect maximized for Pt₅Fe₂/SiO₂. Based on the literature data [56,66], the band at 1799–1804 cm⁻¹ can be assigned to nitrosyl species adsorbed on Fe^{δ+} sites. Terminal Pt nitrosyls also may contribute to this band, as seen in Fig. 11, spectrum 1; however, we can safely assume that the contribution from these species is relatively small, because only a very low-intensity band was detected in Pt/SiO₂. Finally, the band observed in the spectra of the bimetallic catalysts at 1750–1755 cm⁻¹ can be assigned to NO adsorbed on fully reduced Fe sites [56,66]. The presence of some fraction of fully reduced Fe in these bimetallic samples suggests that Pt promoted the reduction of Fe at relatively low temperatures, consistent with earlier literature reports [54]. The intensity of the band corresponding to the fully reduced Fe sites was higher for the Pt₅Fe₂/SiO₂ sample. Since

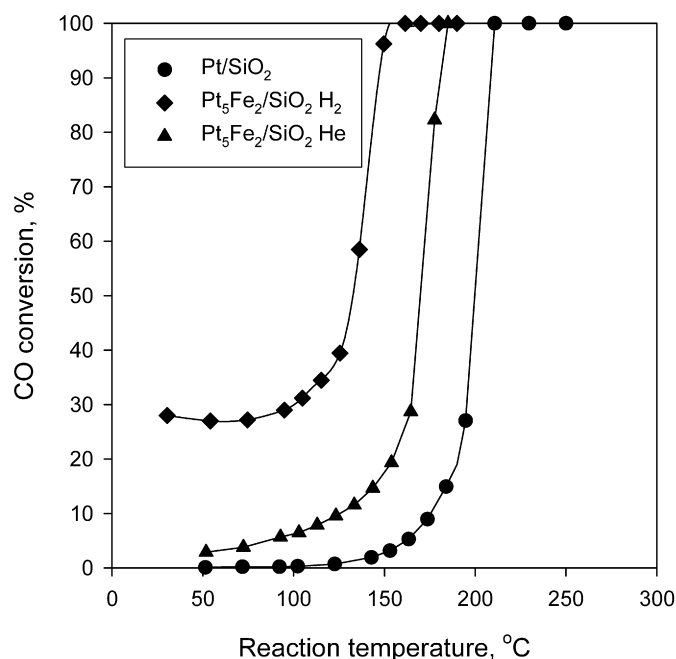


Fig. 12. CO conversions observed during the oxidation of CO in air over (◆) Pt₅Fe₂/SiO₂ pretreated in H₂ at 350 °C, (▲) Pt₅Fe₂/SiO₂ pretreated in He at 350 °C, and (●) Pt/SiO₂ pretreated in H₂ at 350 °C. (Conditions: 1% CO, balance air, GHSV of 120,000 ml/g h).

this sample exhibited the largest fraction of bimetallic interactions, this finding suggests that the close proximity between Pt atoms and Fe cations facilitated the Fe reduction in this case.

3.5. Catalytic oxidation of CO

We reported previously that SiO₂-supported PtFe bimetallic samples were more active than Pt/SiO₂ not only for the selective oxidation of CO in the presence of H₂ (PROX), but also for the oxidation of CO in air [12]. This finding indicates that Fe improves the catalytic performance of Pt in both highly reducing and oxidizing environments. The structural data that we report in this paper provide more insight into the differing catalytic performance of various PtFe catalysts and into the various structure–catalytic activity relationships. For example, our structural data demonstrate that surface species with completely different structures can be formed as a result of the thermal treatment of the Pt₅Fe₂(COD)₂(CO)₁₂/SiO₂ sample. The treatment in He led to the formation of small Pt clusters and Fe oxide-like species, whereas the treatment in H₂ led to the formation of PtFe bimetallic nanoparticles. These two different structures have substantially different catalytic properties for the oxidation of CO in air. Catalytic activity measurements shown in Fig. 12 clearly indicate that the H₂-treated sample was more active than the He-treated sample. These findings suggest that the reaction proceeded at significantly higher rates over PtFe bimetallic sites than over either monometallic Pt or even highly dispersed Pt clusters, some of which may be located in close proximity to Fe oxide-like species. This comparison leads us to the conclusion that *the presence of Pt–Fe bimetallic interactions is a crucial factor triggering the high activity of Pt*

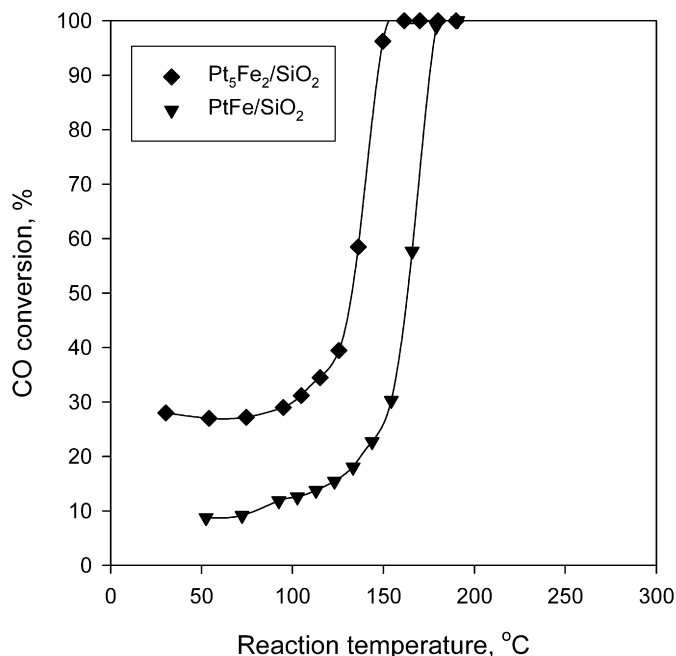


Fig. 13. CO conversions observed during the oxidation of CO in air over (◆) Pt₅Fe₂/SiO₂ and (▼) PtFe/SiO₂ pretreated in H₂ at 350 °C. (Conditions: 1% CO, balance air, GHSV of 120,000 ml/g h.)

for this reaction. Comparing the activities of the cluster-derived Pt₅Fe₂/SiO₂ and the conventional PtFe/SiO₂ samples (Fig. 13) supports this conclusion, because the Pt₅Fe₂/SiO₂ sample, with the larger fraction of Pt–Fe contributions, was the more active of the two samples.

Enhanced catalytic activity can be achieved either by decreasing the activation barrier in the rate-determining step or by facilitating a new pathway for the reaction. Previous detailed investigations of the CO oxidation mechanism have established that this reaction over Pt-based catalysts involves three major steps consistent with a Langmuir–Hinshelwood mechanism [67]:



It has been suggested that the enhanced rate of this reaction over various bimetallic catalysts, including the PtFe combination, can be attributed to the initiation of a noncompetitive dual-site mechanism. According to this scheme, close proximity between Pt and Fe sites is required for the reaction to proceed through the interaction of CO molecules adsorbed on Pt with oxygen adsorbed on Fe⁰ or Fe^{δ+} sites [40,68–70].

Based on the experimental data reported in the previous sections, we can correlate the CO oxidation activity not only with the presence of bimetallic interactions in the samples, but also with the electronic state of Pt and the strength of CO adsorption on the Pt sites. Our FTIR data indicate that in Pt₅Fe₂/SiO₂ (the most active catalyst for this reaction), both the ν_{CO} and ν_{NO} bands underwent a red shift indicative of the presence of electron-rich Pt sites formed due to the interactions with Fe

species. The adsorption of CO on these Pt^{δ-} sites leads to elongation of the C=O bond, which in turn could contribute to the enhanced catalytic activity during the CO oxidation reaction [71]. Similar correlations between the ν_{CO} shift and catalytic activity have been reported previously for other Pt-based catalysts [72]. Furthermore, our data show that the activity for the oxidation of CO is strongly correlated with the strength of CO adsorption on the surface of platinum (Fig. 9); in fact, the most active Pt₅Fe₂/SiO₂ sample is characterized by the highest rate of CO desorption. Therefore, we conclude that *the more weakly adsorbed CO species are activated more easily during CO oxidation*. This suggestion is consistent with theoretical calculations demonstrating a correlation between the chemisorption energies of CO and O₂ molecules and the activation of these reactants. Strong bonding of these molecules to the metal surface leads to higher energy barriers for the CO oxidation reaction [73,74].

4. Conclusions

In this work, FTIR and EXAFS spectroscopy measurements were used to characterize the adsorption of a Pt₅Fe₂(COD)₂-(CO)₁₂ cluster on SiO₂ and the surface species formed after ligand removal in He and H₂. The weak interactions between the cluster and the SiO₂ surface observed initially became stronger with time, as indicated by the displacement of some CO ligands from the supported cluster, most likely due to interactions with the silanol groups. The PtFe bimetallic interactions remained largely intact during this process, whereas the Pt₅Fe₂ cluster core showed some signs of an initial breakup.

Removal of the CO ligands in He and H₂ by TPD caused increased CO desorption from the SiO₂-supported Pt₅Fe₂(COD)₂-(CO)₁₂ species when H₂ was used, indicating that a cleaner catalyst surface could be obtained in this case. The EXAFS data characterizing the resulting metal species in decarbonylated samples indicate that their structures depended largely on the pretreatment atmosphere. When He was used for the treatment, the formation of highly dispersed Pt clusters and oxide-like Fe species was observed. In contrast, treatment in H₂ led to the formation of PtFe bimetallic nanoparticles with an average size of approximately 1 nm, likely through the condensation of several Pt₅Fe₂ cluster units. A PtFe/SiO₂ reference sample prepared by co-impregnation from monometallic Pt and Fe precursors and treated in H₂ at 350 °C also exhibited some bimetallic character, but was less dispersed than the cluster-derived sample and had greater segregation between the two metals.

Adsorption of probe molecules (i.e., CO and NO) on the different bimetallic samples indicated the presence of electron-rich Pt sites. The formation of these sites can be attributed to electronic interactions between Pt and Fe atoms, which were maximized when the Pt₅Fe₂(COD)₂(CO)₁₂ cluster was used as a precursor. Moreover, IR data indicate that Fe in bimetallic samples was present in both the Fe^{δ+} and Fe⁰ forms, suggesting that Pt facilitates the reduction of Fe. The fraction of fully reduced Fe sites was greater in the Pt₅Fe₂/SiO₂ sample characterized by the largest fraction of Pt–Fe interactions, implying that close proximity between the two metals is an important

factor affecting the reduction process. Furthermore, hydrogen chemisorption data indicated significantly reduced chemisorptive properties in the samples with the greater number of Pt–Fe interactions. The strength of CO adsorption on these bimetallic samples also appeared to follow a similar pattern.

Both the Pt₅Fe₂/SiO₂ and PtFe/SiO₂ samples were more active for the oxidation of CO in air when compared to monometallic Pt/SiO₂. The enhanced catalytic activity depends strongly on the structure of the surface species formed, the fraction of Pt–Fe interactions in the sample, the degree of electronic interactions between the metals, and the strength of the CO adsorption. All of these factors were enhanced when a cluster precursor was used and treated in H₂, thus leading to a more active catalyst than that obtained through a conventional preparation method.

Acknowledgments

This work was supported by the U.S. Department of Energy, Office of Basic Energy Sciences (grants DE-FG02-05ER15731 and DE-FG02-05ER14980). The authors thank Dr. Markus Hoelzle and Mr. David Artrip (BASF) for useful technical discussions. Portions of this research were carried out at the Stanford Synchrotron Radiation Laboratory (SSRL), a national user facility operated by Stanford University on behalf of the U.S. Department of Energy, Office of Basic Energy Sciences. The authors are grateful to the beamline staff at SSRL for their assistance. The EXAFS data were analyzed with the XDAP software developed by XAFS Services International. The authors also thank Professor B.C. Gates for providing laboratory equipment used to prepare samples for EXAFS characterization.

References

- [1] J.H. Sinfelt, *Bimetallic Catalysts, Discoveries, Concepts and Applications*, Wiley, New York, 1983.
- [2] O.S. Alexeev, B.C. Gates, *Ind. Eng. Chem. Res.* 42 (2003) 1571.
- [3] L.B. Ortiz-Soto, O.S. Alexeev, M.D. Amiridis, *Langmuir* 22 (2006) 3112.
- [4] R.D. Adams, *J. Organomet. Chem.* 600 (2000) 1.
- [5] S. Hermans, R. Raja, J.M. Thomas, B.F.G. Johnson, G. Sankar, D. Gleeson, *Angew. Chem. Int. Ed.* 40 (2001) 1211.
- [6] R. Raja, G. Sankar, S. Hermans, D.S. Shephard, S. Bromley, J.M. Thomas, *Chem. Commun.* (1999) 1571.
- [7] M. Mavrikakis, B. Hammer, J.K. Nørskov, *Phys. Rev. Lett.* 81 (1998) 2819.
- [8] J.R. Kitchin, J.K. Nørskov, M.A. Barteau, J.G. Chen, *J. Chem. Phys.* 120 (2004) 10240.
- [9] Y. Xu, A.V. Ruban, M. Mavrikakis, *J. Am. Chem. Soc.* 126 (2004) 4717.
- [10] R.D. Adams, F.A. Cotton, *Catalysis by Di- and Polynuclear Metal Cluster Complexes*, Wiley–VCH, New York, 1998.
- [11] R.D. Adams, I. Arafat, G. Chen, J.C. Lii, J.G. Wang, *Organometallics* 9 (1990) 2350.
- [12] A. Siani, B. Captain, O.S. Alexeev, E. Stafyla, A.B. Hungria, P.A. Midgley, J.M. Thomas, R.D. Adams, M.D. Amiridis, *Langmuir* 22 (2006) 5160.
- [13] D.K. Captain, M.D. Amiridis, *J. Catal.* 184 (1999) 377.
- [14] B.K. Teo, P.A. Lee, *J. Am. Chem. Soc.* 101 (1979) 2815.
- [15] F.B.M. Duivenvoorden, D.C. Koningsberger, Y.S. Uh, B.C. Gates, *J. Am. Chem. Soc.* 108 (1986) 6254.
- [16] D. Braga, F. Grepioni, A.G. Orpen, *Organometallics* 12 (1993) 1481.
- [17] M. Vaarkamp, J.C. Linders, D.C. Koningsberger, *Physica B* 208–209 (1995) 159.
- [18] D.C. Koningsberger, in: C.A. Melendres, A. Tadjeddine (Eds.), *Synchrotron Techniques in Interfacial Electrochemistry*, Kluwer, Dordrecht, 1994.
- [19] E.A. Stern, *Phys. Rev. B* 48 (1993) 9825.
- [20] E.O. Brigham, *The Fast Fourier Transform*, Prentice Hall, Englewood Cliffs, NJ, 1974.
- [21] P.S. Kirilin, F.B.M. van Zon, D.C. Koningsberger, B.C. Gates, *J. Phys. Chem.* 94 (1990) 8439.
- [22] J.B.A.D. van Zon, D.C. Koningsberger, H.F.J. van't Blik, D.E. Sayers, *J. Chem. Phys.* 82 (1985) 5742.
- [23] O.S. Alexeev, M. Shelef, B.C. Gates, *J. Catal.* 164 (1996) 1.
- [24] M. Vaarkamp, Ph.D. thesis, Eindhoven University, The Netherlands, 1993.
- [25] F.W. Lytle, D.E. Sayers, E.A. Stern, *Physica B* 158 (1988) 701.
- [26] D.C. Koningsberger, B.L. Mojet, G.E. van Dorssen, D.E. Ramaker, *Top. Catal.* 10 (2000) 143.
- [27] J.H. Sinfelt, in: Y. Iwasawa (Ed.), *X-Ray Absorption Fine Structure for Catalysts and Surfaces*, World Scientific Publishing, Singapore, 1996.
- [28] F. Hugues, J.M. Basset, Y.B. Taarit, A. Chiplin, M. Primet, D. Rojas, A.K. Smith, *J. Am. Chem. Soc.* 104 (1982) 7020.
- [29] Y.I. Ermakov, B.N. Kuznetsov, V.A. Zakharov, *Studies in Surface Science and Catalysis*, in: *Catalysis of Supported Complexes*, vol. 8, Elsevier, Amsterdam, 1981.
- [30] B. Besson, B. Moraweck, A.K. Smith, J.M. Basset, R. Psaro, A. Fusi, R. Ugo, *J. Chem. Soc. Chem. Commun.* (1980) 569.
- [31] A.K. Smith, B. Besson, J.M. Basset, R. Psaro, A. Fusi, R. Ugo, *J. Organomet. Chem.* 192 (1980) C31.
- [32] M. Deeba, B.C. Gates, *J. Catal.* 67 (1981) 303.
- [33] P.L. Watson, G.L. Schrader, *J. Mol. Catal.* 9 (1980) 125.
- [34] O.S. Alexeev, B.C. Gates, *Top. Catal.* 10 (2000) 273.
- [35] B.C. Gates, *Chem. Rev.* 95 (1995) 511.
- [36] A.K. Hughes, K. Wade, *Coord. Chem. Rev.* 197 (2000) 191.
- [37] A.W. Ehlers, S. Dapprich, S.F. Vyboishchikov, G. Frenking, *Organometallics* 15 (1996) 105.
- [38] T.A. Barckholtz, B.E. Bursten, *J. Organomet. Chem.* 596 (2000) 212.
- [39] F. Delbecq, *Surf. Sci.* 389 (1997) L1131.
- [40] A. Sirirajuraphan, J.G. Goodwin, R.W. Rice, *J. Catal.* 224 (2004) 304.
- [41] G.L. Gutsev, C.E. Bauschlicher, L. Andrews, *J. Chem. Phys.* 119 (2003) 3681.
- [42] H. Xu, J. Shi, Z. Guo, *Ranliao Huaxue Xuebao* 22 (1994) 70.
- [43] R.W.G. Wyckoff, *Crystal Structures*, Wiley, New York, 1967.
- [44] R.L. Blake, R.E. Hessevick, T. Zoltai, L.W. Finger, *Am. Mineral.* 51 (1966) 123.
- [45] B.A. Wechsler, D.H. Lindsley, C.T. Prewitt, *Am. Mineral.* 69 (1984) 754.
- [46] S. Calvin, S.X. Luo, C. Caragianis-Broadbridge, J.K. McGuinness, E. Anderson, A. Lehman, K.H. Wee, S.A. Morrison, L.K. Kurihara, *Appl. Phys. Lett.* 87 (2005) 233102.
- [47] M.S. Nashner, A.I. Frenkel, D. Somerville, C.W. Hills, J.R. Shapley, R.G. Nuzzo, *J. Am. Chem. Soc.* 120 (1998) 8093.
- [48] B.J. Kip, F.B.M. Duivenvoorden, D.C. Koningsberger, R. Prins, *J. Catal.* 105 (1987) 26.
- [49] R.B. Gregor, F.W. Lytle, *J. Catal.* 63 (1980) 476.
- [50] E.S. Shpiro, R.W. Joyner, K.M. Minachev, D.A. Pudney, *J. Catal.* 127 (1991) 366.
- [51] C. Kittel, *Introduction to Solid State Physics*, Wiley, New York, 1996.
- [52] P.V. Jasen, E.A. Gonzales, N.J. Castellani, A. Juan, *Phys. Rev. B* 71 (2005) 235422.
- [53] J.C.S. Wu, T.-S. Cheng, C.-L. Lai, *Appl. Catal. A* 314 (2006) 233.
- [54] L. Guzzi, *Catal. Rev. Sci. Eng.* 23 (1981) 329.
- [55] O.S. Alexeev, G.W. Graham, D.-W. Kim, M. Shelef, B.C. Gates, *Phys. Chem. Chem. Phys.* 1 (1999) 5257.
- [56] C. Johnston, N. Jorgensen, C.H. Rochester, *J. Chem. Soc. Faraday Trans. 1* 84 (1988) 309.
- [57] G. Blyholder, *J. Phys. Chem.* 68 (1964) 2772.
- [58] L.H. Little, *Infrared Spectra of Adsorbed Species*, Academic Press, London, 1966.
- [59] C. Mihut, C. Descorme, D. Duprez, M.D. Amiridis, *J. Catal.* 212 (2002) 125.
- [60] J.H. Sinfelt, G.D. Meitzner, *Acc. Chem. Res.* 26 (1993) 1.

- [61] N. Dimakis, H. Iddir, R.R. Diaz-Morales, R. Liu, G. Bunker, E.-H. Chung, E.S. Smotkin, *J. Phys. Chem. B* 109 (2005) 1839.
- [62] F. Delbecq, B. Moraweck, L. Verite, *Surf. Sci.* 396 (1998) 156.
- [63] C. Xu, B.E. Koel, *Surf. Sci.* 310 (1994) 198.
- [64] A. Atli, M. Abon, P. Beccat, J.C. Bertolini, B. Tardy, *Surf. Sci.* 302 (1994) 121.
- [65] A.A. Davydov, *Infrared Spectroscopy of Adsorbed Species on the Surface of Transition Metal Oxides*, Wiley, Chichester, 1990.
- [66] H. Bandow, T. Onishi, K. Tamaru, *Chem. Lett.* (1978) 83.
- [67] T. Engel, G. Ertl, *Adv. Catal.* 28 (1979) 2.
- [68] M. Kotobuki, A. Watanabe, H. Uchida, H. Yamashita, M. Watanabe, *J. Catal.* 236 (2005) 262.
- [69] X. Liu, O. Korotkikh, R.J. Farrauto, *Appl. Catal. A* 226 (2002) 293.
- [70] H. Liu, A.I. Kozlov, A.P. Kozlova, T. Shido, Y. Iwasawa, *Phys. Chem. Chem. Phys.* 1 (1999) 2851.
- [71] C. Pedrero, T. Waku, E. Iglesia, *J. Catal.* 233 (2005) 242.
- [72] O.S. Alexeev, S.Y. Chin, M.H. Engelhard, L. Ortiz-Soto, M.D. Amiridis, *J. Phys. Chem. B* 109 (2005) 23430.
- [73] Z.-P. Liu, P. Hu, *Top. Catal.* 28 (2004) 71.
- [74] Z.-P. Liu, P. Hu, *J. Chem. Phys.* 115 (2001) 4977.